

SURFACE IMAGING OF PROXIMA B AND OTHER EXOPLANETS: TOPOGRAPHY, BIOSIGNATURES, AND ARTIFICIAL MEGA-STRUCTURES

S. V. BERDYUGINA^{1,2}, J. R. KUHN²

Draft version November 2, 2017

ABSTRACT

Seeing oceans, continents, quasi-static weather, and other surface features on exoplanets may allow us to detect and characterize life outside the solar system. The Proxima b planet resides within the stellar habitable zone allowing for liquid water on its surface, and it may be Earth-like. However, even the largest planned telescopes will not be able to resolve its surface features directly. Here, we demonstrate an inversion technique to image indirectly exoplanet surfaces using observed unresolved reflected light variations over the course of the exoplanets orbital and axial rotation: ExoPlanet Surface Imaging (EPSI). We show that the reflected light curve contains enough information to detect both longitudinal and latitudinal structures and to map exoplanet surface features. We demonstrate this using examples of Solar system planets and moons as well as simulated planets with Earth-like life and artificial megastructures. We also describe how it is possible to infer the planet and orbit geometry from light curves. In particular, we show how albedo maps of Proxima b can be successfully reconstructed for tidally locked, resonance, and unlocked axial and orbital rotation. Such albedo maps obtained in different wavelength passbands can provide "photographic" views of distant exoplanets. We estimate the signal-to-noise ratio necessary for successful inversions and analyse telescope and detector requirements necessary for the first surface images of Proxima b and other nearby exoplanets.

Subject headings: planetary systems — exoplanets

1. INTRODUCTION

Resolving surface features (e.g., continents) or global weather patterns on even the nearest exoplanets through *direct imaging* requires optical systems many km in size – this will not happen soon. On the other hand, emitted and reflected planet light has been detected from exoplanet host stars by different observing techniques in a few cases. The *Spitzer* space telescope measured IR light curves of hot Jupiters and detected enhanced emission longitudes ("hot spots") in their atmospheres (e.g., Harrington et al. 2006; Knutson 2007; Cowan & Agol 2008; Crossfield et al. 2010). However, the latitudinal information could not be yielded from these data. High-precision polarimetry has provided first albedo and color measurements for a hot Jupiter (Berdyugina et al. 2008, 2011). Similarly, CoRoT, *Kepler* and *Hubble* telescopes achieved sensitivity to detect optical and near UV reflected light curves from hot Jupiters (e.g., Snellen et al. 2009; Demory et al. 2011; Faigler & Mazeh 2015; Evans et al. 2013).

Model solutions for albedo maps and orbital parameters based on reflected flux or polarization light curves have been previously demonstrated for exoplanets (e.g., Cowan et al. 2009; Fluri & Berdyugina 2010; Kawahara & Fujii 2011; Fujii & Kawahara 2012; Schwartz et al. 2016). With an independent formalism presented in this paper – ExoPlanet Surface Imaging (EPSI) – we confirm some of the conclusions of those papers and elaborate applications for planets with and without clouds, with seasonal variations, photosynthetic organism colonies and artificial structures built by advanced civilizations. Multi-

wavelength observations of such planets may enable detection of primitive and even advanced exolife. Unlike Cowan et al. (2009) we can recover not only longitudinal information but also plenty of latitudinal information on exoplanet surfaces. Also, in contrast to Fujii & Kawahara (2012), our modeling suggests that large telescope apertures are needed to infer surface albedo maps. For example, mapping Proxima b requires a telescope with the diameter at least 12 m. This paper focuses on realistic models and expectations for mapping the nearest exoplanets.

We show that moderate signal-to-noise ratio (SNR) time-series photometry of an exoplanet's reflected light can yield a 2D surface map of its albedo using an inversion technique. Reflected light photometry (or/and polarimetry) of exoplanets when the planet rotation axis is inclined with respect to the orbit plane normal direction offers the greatest possibility for mapping the exoplanet surface or seeing stable atmospheric structure with surprisingly high spatial resolution. Our numerical technique follows similar algorithms used for mapping starspots (Berdyugina 1998; Berdyugina et al. 1998, 2002).

The recent discovery of the nearest exoplanet Proxima b (Anglada-Escudé et al. 2016) is an opportunity for obtaining the first surface (and/or weather) images of a possibly Earth-like exoplanet. Here we investigate in some detail the orbit-rotation parameter space relevant to Proxima b. We estimate the necessary SNR of the data and evaluate how it can be achieved with future telescopes.

The paper is structured as follows. In Section 2, we describe our direct model and an inversion algorithm. In Section 3, we present simulations and inversions for exoplanets with Earth-like albedo distribution due to ocean

¹ Kiepenheuer Institut für Sonnenphysik, Schöneckstrasse 6, D-79104 Freiburg, Germany; sveta@leibniz-kis.de

² Institute for Astronomy/Maui, University of Hawaii, 34 Ohia Ku St., Pukalani, HI 96768, USA; kuhn@ifa.hawaii.edu

and land topography. We show that, under some circumstances, there is sufficient information in the reflected light curve to resolve an accurate map of the exoplanet surface on the scale of subcontinents. We also discuss limitations due to data noise, weather system evolution, and seasonal variations in the cloud and surface albedo. In Section 4, we present inversions for Solar system planets and moons as analogs of exoplanets. We can recover global circulation cloud patterns on Jupiter, Neptune, and Venus, as well as surface features on the Moon, Mars, Io and Pluto. In Section 5, we present models for spectral (broad-band) imaging of exoplanets with Earth-like life and demonstrate that photosynthetic biosignatures and surface composition can be unambiguously detected with our technique. We also model hypothetical planets with global artificial structures which can be detected under certain circumstances. In Section 6, we present simulations and inversions for the Proxima b planet assuming tidally locked orbits at the 1:1 and 2:3 resonances. In Section 7, we investigate and formulate observational requirements for the telescope size and scattered light level, in order to obtain spectral images of Proxima b and possible rocky planets in the nearest to the Sun stellar system Alpha Centauri A and B. We find that telescopes in diameter of 12 m or larger and with a high level of scattered light suppression can achieve the required signal-to-noise ratio in planet brightness measurements above the stellar glare background. We also estimate how many Earth-size and super-Earth planets in water-based habitable zones (WHZ) of nearby 3500 AFGKM stars can be imaged with our technique depending on the telescope aperture for a given scattered light background. Finally, In Section 8, we summarize our results and conclusions.

2. MODEL AND INVERSION ALGORITHMS

In this section, we describe the model and the inversion algorithm. The model includes radiation physics and star-planet geometry. The inversion algorithm includes criteria for choosing a unique solution and for evaluating the quality of the recovered image.

The concept of our EPSI technique is evident if we consider a set of high albedo spots at fixed longitude but variable latitude. Figure 1 shows how the latitude information of each reflective spot is encoded in the yearly variation of the peak daily brightness. Each latitude creates a distinct yearly variation profile, while each longitude affects the light curve at a distinct daily temporal phase. It is evident that de-projecting corresponding daily phased brightness measurements over the course of an exoplanet year allows, in principle, reconstruction of the latitude and longitude albedo variation from orbital and rotational sampling.

In fact, assuming that the surface structure does not (or insignificantly) evolve during the time covered by the light curve, this information can be inverted into a 2D map of the surface – an indirect imaging technique that is employed in various remote sensing applications, e.g., asteroid mapping or stellar surface imaging. Fujii & Kawahara (2012) employed this approach combined with the Tikhonov Regularization (TR) inversion algorithm, which minimized discrepancies between the model and observations by choosing the solution with the minimum albedo gradient, i.e., it results in the smoothest map solution. Here, we describe an algorithm employing the Oc-

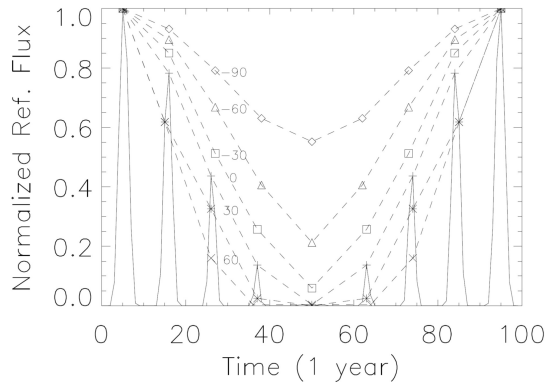


FIG. 1.— Reflected light curves for an exoplanet with a single high albedo spot as a Gaussian with the width about 5 degrees. The planet has an orbit period of 100 time units with a diurnal period of 10. The solid curve shows the light curve for an equatorial spot which goes in and out of view due to axial rotation and is illuminated fully or in part due to orbital motion. When the spot is moved to other latitudes, the peak amplitudes are changed. Symbols joined by dashed lines show the corresponding peak brightness for a spot located at the marked planetary latitudes. The observer here is located 90° from the planet rotation axis and the normal to the plane of the orbit is 45° from the rotation axis. These calculations assume a simple $\cos\theta$ albedo angle dependence.

camian Approach (OA) inversion technique (Berdyugina 1998). It is based on the Principal Component Analysis (PCA) which does not constrain the solution with any prior specific smoothness properties (see Section 2.2).

2.1. Direct Modeling

2.1.1. Radiation Physics

The reflecting surface of the planet is divided by a grid in longitude and latitude. Each grid pixel is assigned a geometrical albedo value A for a given wavelength or passband and a phase function P defining the angular distribution of the reflected light. Thus, if P is defined, there are $N = N_{\text{lat}} \times N_{\text{lon}}$ unknowns, which comprise an albedo map of the planet with N_{lat} latitudes and N_{lon} longitudes. This generic description of the surface allows us to compute reflected light from various surfaces, including a cloud deck and the planet surface with and without an atmosphere.

Different phase functions can be assigned for different scatterers, e.g., Rayleigh for gas and small particles, Mie for cloud droplets, lab measured BRDF for various surfaces, etc. (e.g., Berdyugina et al. 2016; Berdyugina 2016). For simplicity, initial tests presented in this paper were calculated with the assumption that surface reflection is isotropic, gaseous atmospheric scattering is Rayleigh, $\hat{\mathbf{P}}_{\text{Ray}}$, and cloud particles are spherical droplets, $\hat{\mathbf{P}}_{\text{Mie}}$, if not stated otherwise throughout the paper. In some cases, reflected *flux* spectra from dense (optically thick) high clouds can be described by a composite phase function including a Rayleigh scattering contribution from a thin gaseous atmosphere above the cloud deck and a diffuse, but wavelength-dependent reflected flux from clouds of a given albedo A_c . Hence, to account for clouds, we assume that each planet map pixel can have contributions from clouds and planet surface, with respective filling factors f_c and $1 - f_c$. The corresponding gaseous atmosphere scattering contributions depend on the optical thickness of the atmosphere above

the planet surface and above the cloud deck. Here, we assume that the light scattered by clouds downwards and subsequently reflected by the surface is trapped within the atmosphere and does not reach an external observer (i.e., one cannot "see" through clouds). This approach further simplifies the problem and accelerates inversions.

Multiple scattering is computed by solving iteratively the radiation transfer equations for intensity and polarization, i.e., for the Stokes vector $\mathbf{I} = (I, Q, U, V)^T$ of a given frequency (omitted for clarity) toward the direction defined by two angles ($\mu = \cos \theta$, ψ):

$$\mu \frac{d\mathbf{I}(\tau, \mu, \psi)}{d\tau} = \mathbf{I}(\tau, \mu, \psi) - \mathbf{S}(\tau, \mu, \psi) \quad (1)$$

with the total source function

$$\mathbf{S}(\tau, \mu, \psi) = \frac{\kappa(\tau)\mathbf{B}(\tau) + \sigma(\tau)\mathbf{S}_{\text{sc}}(\tau, \mu, \psi)}{\kappa(\tau) + \sigma(\tau)}, \quad (2)$$

where κ and σ are absorption and scattering opacities, \mathbf{S}_{sc} and \mathbf{B} are the scattering source function and the unpolarized thermal emission, respectively, and τ is the optical depth in the atmosphere with $\tau = 0$ at the top. The formal solution of Eq. (1) is (e.g., Sobolev 1956)

$$\begin{aligned} \mathbf{I}(\tau, \mu, \psi) &= \mathbf{I}(\tau_*, \mu, \psi) e^{-(\tau_* - \tau)/\mu} \\ &+ \int_{\tau}^{\tau_*} \mathbf{S}(\tau', \mu, \psi) e^{-(\tau' - \tau)/\mu} \frac{d\tau'}{\mu}, \end{aligned} \quad (3)$$

where τ_* is either the optical depth at the bottom of the atmosphere for the Stokes vector $\mathbf{I}^+(\tau, \mu, \psi)$ coming from the bottom to the top ($\theta < \pi/2$) or the optical depth at the top of the atmosphere ($\tau_* = 0$) for the Stokes vector $\mathbf{I}^-(\tau, \mu, \psi)$ coming from the top to the bottom ($\theta > \pi/2$).

The scattering source function \mathbf{S}_{sc} is expressed via the scattering phase matrix $\hat{\mathbf{P}}(\mu, \mu'; \psi, \psi')$, depending on the directions of the incident (μ' , ψ') and scattered (μ , ψ) light:

$$\mathbf{S}_{\text{sc}}(\tau, \mu, \psi) = \int \hat{\mathbf{P}}(\mu, \mu'; \psi, \psi') \mathbf{I}(\tau, \mu', \psi') \frac{d\Omega'}{4\pi}. \quad (4)$$

It has contributions from scattering both incident stellar light and intrinsic thermal emission. Their relative contributions depend on the frequency. For instance, for Rayleigh scattering the intensity of the thermal emission of an Earth-like planet in the blue part of the spectrum is negligible compared to that of the scattered stellar light. The phase matrix $\hat{\mathbf{P}}(\mu, \mu'; \psi, \psi')$ is a 4×4 matrix with six independent parameters for scattering cases on particles with a symmetry (e.g., Hansen & Travis 1974). In this paper we employ the Rayleigh and Mie scattering phase matrices but our formalism is valid for other phase functions too.

The Stokes vector of the light emerging from the planetary atmosphere $\mathbf{I}(0, \mu, \psi)$ is obtained by integrating iteratively Equations (2) and (3) for a given vertical distribution of the temperature and opacity in a planetary atmosphere. We solve this problem under the following assumptions:

- 1) the atmosphere is plane-parallel and static;
- 2) the planet is spherically symmetric;
- 3) stellar radiation can enter the planetary atmosphere from different angles and can be polarized;
- 4) an incoming photon is either absorbed or scattered according to opacities in the atmosphere;

5) an absorbed photon does not alter the atmosphere (model atmosphere includes thermodynamics effects of irradiation);

6) photons can be scattered multiple times until they escape the atmosphere or absorbed.

These assumptions expand those in Fluri & Berdyugina (2010), namely that multiple scattering on both molecules and particles is accounted for, stellar irradiation can be polarized and vary with an incident angle, and the planetary atmosphere and surface can be inhomogeneous in both longitude and latitude. Boundary conditions are defined by stellar irradiation at the top, surface reflection at the bottom, and planetary thermal radiation, if necessary. Note that the bottom boundary condition refers to reflection from both the planetary surface and the cloud deck. Depending on the structure of the phase matrix and the boundary conditions, the equations are solved for all or fewer Stokes vector components. Normally it takes 3–15 iterations to achieve a required accuracy (depending on the surface albedo and optical thickness of the atmosphere).

The stellar light is initially approximated by black body radiation with the effective temperature of the star, but nothing prevents us to employ real stellar spectra. Theoretically, the stellar spectrum is removed by normalization to the incident light (like in the case of the Solar system bodies). In reality, however, stellar spectral lines induce irradiation fluctuations and, hence, the signal-to-noise ratio (SNR) variations with wavelength. In Section 7 we show realistic calculations of the SNR for the nearest exoplanet(s) in the Alpha Centauri system in broad photometric bands that is feasible in the near future.

For cloudless Earth-like planets, we used a standard Earth atmosphere (McClatchey et al. 1972), for which we computed Rayleigh scattering opacities and optical thickness depending in the height in the atmosphere. For cloudy planets, we assumed an atmosphere of a given optical thickness above clouds, while cloud particles scatter light according to the chosen phase function.

Using such atmospheres, we have computed reflected radiation for a set of incoming and outgoing angles. Since the amount of scattered light in a cloudless atmosphere depends on the surface albedo, we also computed the outgoing radiation for a set of surface albedo values. These pre-computed sets were used for simulations and inversions of light curves. It is obvious that the optical thickness of the atmosphere influences the visibility of the surface. Therefore, for thicker atmospheres there is less information in the light curve on the surface albedo, and this has to be accounted for while carrying out inversions. Time-dependent reflected light curves were computed by integrating local Stokes parameters over the planetary surface at different rotational and orbital phases. Various levels of Poisson (photon) noise were introduced into the theoretical light curves to imitate observations.

2.1.2. Star and Planet Geometry

If the planet is angularly resolved from the star by direct imaging with a large enough telescope, its flux can be measured directly. This also implies that the planet flux should exceed background stellar scattered light (including telescope scattering and sky background) at the angular separation between the planet and the star. If

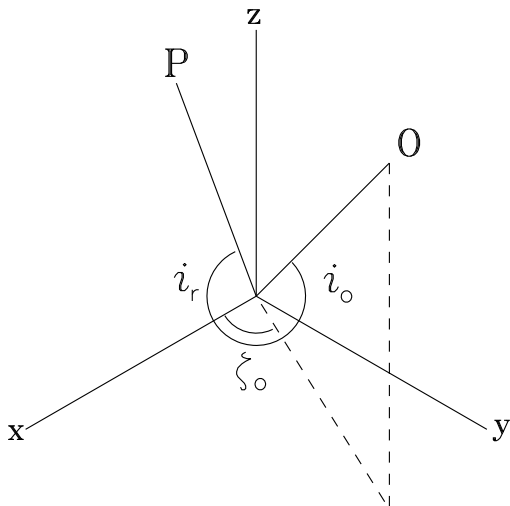


FIG. 2.— Geometry of a planet orbiting a star: y and z axis are in the plane of the sky, x axis is toward the observer (perpendicular to the page). Planet axis inclination $i_r = 60^\circ$, orbit normal inclination $i_o = 30^\circ$, and orbit normal azimuth $\zeta_o = 30^\circ$,

the star-planet system is unresolved, the stellar light is added to the planet reflected flux. Since the stellar flux is in general variable (e.g., due to magnetic activity or oscillations) during the planet orbital period, it is important to have observing tools to disentangle planetary and stellar variability. In general this is possible because 1) the starlight spectral and polarization characteristics are different from those of the planet, and 2) if the star is resolved from the planet, its variability can be separately measured.

We define the star-planet geometry in a Cartesian frame with the axis x toward observer and y and z in the plane of sky (Fig. 2). The planet is assumed to rotate around its axis and orbits its star with different periods, P_r and P_o , respectively.

The rotational axis of the planet is generally inclined with respect to the observer with the angle i_r . Thus, the xyz location on the planet surface is transformed into $x'y'z'$ by rotation by the angle i_r toward the observer. Here, x' is the cosine of the angle between the local normal and the direction to the observer at a given phase, which defines the visibility function V : the pixel is visible to the observer if V is positive, cf. $x' > 0$.

The normal direction to the orbit plane is defined by the inclination angle toward the observer i_o and an azimuth angle ζ_o around axis z (within xy -plane). To compute the amount of stellar illumination, we are interested in knowing the direction toward the star for any planet pixel at any given phase. We assume that the planet is far enough from the star to neglect the stellar solid angle, i.e., radiation coming from the star is unidirectional. Thus, the (x_o, y_o, z_o) direction to the star at a given orbital phase φ_o is transformed into $x'_o y'_o z'_o$ by rotations first by the angle i_o and then by the angle ζ_o (Fig. 2). The cosine between the local normal to the planet surface and the direction toward the star in the observer reference frame defines the illumination function L : the pixel is illuminated by the star if L is positive, i.e. $x'_o x'_o + y'_o y'_o + z'_o z'_o > 0$.

The planet reflected flux for given orbital and rota-

tional phases is computed by integrating the intensity of the reflected light over the set of visible pixels weighted by the pixel area, albedo and illumination fraction. For anisotropic reflection (scattering), it is also weighted by the phase function.

2.2. Inversion Algorithm

Recovering a planet surface albedo distribution from a time series of flux measurements requires solving an ill-posed problem:

$$D = FS, \quad (5)$$

where D is a column vector containing M observations, S is a column vector containing N pixels on the planetary surface (in longitude and latitude), and F is the response operator expressed as an $N \times M$ matrix. The matrix F determines transformation of a planet image into a data or model light curve. It includes all the radiation physics and geometry described in the previous section. Thus our task is to obtain the albedo map S from the data D under the assumptions included into F .

A simple inversion of the matrix F could provide an exact solution if $N = M$, but the solution will be noisy and unstable due to noise in the data. Alternatively, this problem can be solved (also for the case $N \neq M$) by maximizing the overall probability of obtaining the observed data (the likelihood function). However, to avoid fitting the data noise, the overall probability has to be reduced to some "reasonable" level, which leads to multiple possible solutions for a given probability (likelihood). The choice of the probability density function to calculate the likelihood function and the solution "goodness" criterion define the inversion algorithm and the solution itself.

Here we apply an Occamian Approach (OA) algorithm inspired by the "Occam's razor" principle and having been employed for mapping stellar surface brightness from time series of both spectral line profiles and the stellar flux (e.g., Berdyugina et al. 1998, 2002). In contrast to the broadly used Maximum Entropy (ME) and Tikhonov Regularization (TR) methods, the OA algorithm does not define an *a priori* quality of the solution, such as minimum information (ME) or maximum smoothness (TR). Instead, the OA chooses a solution \tilde{S} with the information content equal to that in the data by means of a global maximization of the probability to obtain the observed light curve with the minimum number of significant principal components (see details in Berdyugina 1998). We use the Poisson function to compute the likelihood function and the information content in the data.

2.3. Inversion Quality

To characterize the overall success of the inversion we define an Inversion Quality (IQ) parameter as follows. First, we transform an image S into a "binary" form using a threshold albedo, A_T (e.g., 0.1): $S(A \geq A_T) = 1$ and $S(A < A_T) = 0$. We do this for both the original (S) and recovered (\tilde{S}) images. This operation selects either bright or dark features in the images. Then, using these transformed images, we compute the IQ parameter per cent as follows:

$$IQ = \frac{100\%}{N} \sum_{i=1}^N [S_i \tilde{S}_i + (1 - S_i)(1 - \tilde{S}_i)]. \quad (6)$$

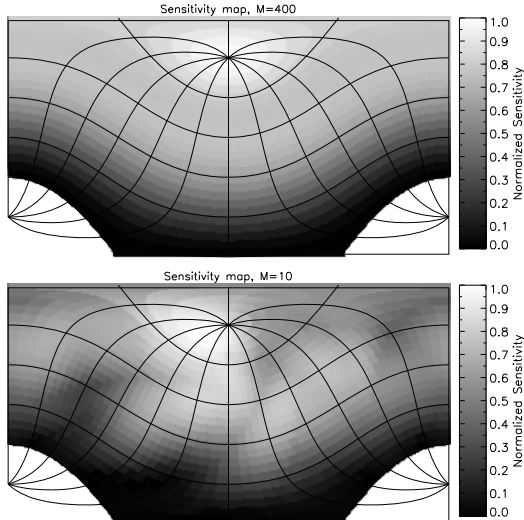


FIG. 3.— Sensitivity maps for model cases with large ($M=400$) and small ($M=10$) amount of data. Observed phases are evenly distributed over the orbital period. The model geometry is the same as in Fig. 2. A lack of measurements results in a “spotty” pattern of the sensitivity. Lower latitudes lack information because of smaller projection area and sparse sampling.

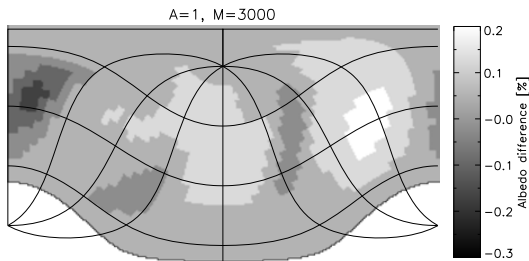


FIG. 4.— Distribution of deviations from the true albedo values $A = 1$ for a model with $i_r = 60^\circ$, $i_o = 30^\circ$, and $\zeta_o = 60^\circ$ shown in Fig. 2 and $M=3000$ as in models EN3000 and ES3000 (see Table 1.)

Thus, IQ is the percentage of pixels in the recovered map having the albedo range coinciding with that in the original map. It is obvious that the IQ parameter depends on the chosen albedo threshold. We found however that for a successful inversion IQ variations with the threshold near the center of the albedo value distribution are not large. In the following section when discussing the inversion results, we will use the threshold albedo $A_T = 0.1$.

Another informative characteristic of the inversion success is the standard deviation (SD) of the recovered map with respect to the input map normalized to the maximum albedo and expressed in percent. This provides an overall measure of the map goodness.

We also compute a sensitivity map in order to evaluate a relative distribution of the available information over the planetary surface. It is composed of products of the visibility and illumination functions summed over all observed phases:

$$\hat{S}_i = \sum_{j=1}^M V_{ij} L_{ij}, \quad (7)$$

where $i = 1, N$ runs over all planet pixels. Thus, \hat{S}_i is proportional to the number of photons reflected toward the observer by the i -th pixel during the total observ-

TABLE 1
TEST INVERSION MODELS FOR AN
EARTH-LIKE PLANET

Model	M_{rot}	M_{ph}	SNR	IQ [%]	SD [%]
EN3000	60	50	200	89	10
ES3000	60	50	200	89	15
EN200	20	10	200	87	11
EN400	20	20	20	80	13

ing time, which defines the error of the restored pixel’s albedo. In Fig. 3 two sensitivity maps are shown for model cases with large and small amount of data. When data sampling is sparse, large gaps in the sensitivity map become apparent. Since the geometry of the planetary orbit and the rotational axis direction with respect to the observer are fixed for a given exoplanet, the sensitivity map helps to optimize data sampling for the best inversion result.

One more way to characterize the quality of the recovered map is to carry out inversion of a light curve for a uniform albedo map (e.g., $A = 1$) with the same set of the sampled phases and SNR as in the observed light curve. The resulting recovered map \tilde{S}_1 provides a distribution of expected deviations from the true albedo values for each pixel. These include limitations due to data sampling, visibility and illumination geometry, SNR, and the choice of the solution “goodness” criterion. Figure 4 shows an example inversion for the $A = 1$ map.

3. EXO-EARTH ALBEDO INVERSIONS

In this section we present example simulations and inversions for an Earth-like planet with continents, ocean and ice caps which allow for large albedo variations across the planetary surface. We demonstrate how the information encoded in the reflected light curve helps to resolve an accurate map of the exoplanet surface on the scale of continents. We also discuss limitations due to data noise, weather system evolution, and seasonal variations in the cloud and surface albedo. We characterize inversion results with the quality parameters introduced in Section 2.3 and investigate how the quality can be maximized. We suggest that further improvements in the recovered image quality can be achieved by using polarized light curves in addition to the flux measurements. Such data may be useful for obtaining other local parameters, like the phase function.

In our tests, we vary the number of planet rotations per orbital period M_{rot} and the number of observed phases per planet rotation M_{ph} as well as SNR, geometrical parameters and cloud cover. As explained earlier, the total number of measurements is $M = M_{\text{rot}} M_{\text{ph}}$.

We employ monthly Earth maps produced by the NASA Earth Observatory (NEO) satellite missions (<https://earthobservatory.nasa.gov/>). The geometrical albedo maps with no clouds are used in Section 3.1. The effect of seasonal surface albedo variations is analyzed in Section 3.2. To study the effect of variable cloud cover, we analyzed a combination of the cloudless albedo maps and monthly cloud cover maps weighted by corresponding filling factors in Section 3.3.

We have rebinned the maps to the $6^\circ \times 6^\circ$ grid, simulated light curves and carried out inversions as described

in Section 2. The employed models are summarized in Table 1. They are all computed with $i_r = 60^\circ$, $i_o = 30^\circ$, and $\zeta_o = 60^\circ$.

3.1. Cloudless Exo-Earths

First, we verify that we can resolve planet surface features in both longitude and latitude under favorable conditions, i.e., we assume data with sufficient SNR, sufficient number of measurements, a favorable (but not unlikely) planet geometry, optically thin (at a given wavelength) atmosphere, and no clouds. Inversions for less favorable scenarios are presented in subsequent subsections. We use the $6^\circ \times 6^\circ$ surface grid for inversions, as it yields reasonable surface resolution and a comfortable computational effort. This grid has $N = 1800$ pixels (when $i_r = 90^\circ$) which implies that the measurement number M should be of the same order for a realistic solution. We note that our algorithm also converges when $N > M$ but errors increase.

For the first test, we assume that it is possible to obtain planet brightness measurements at 50 evenly spaced axial rotational phases with a SNR=200. The orbital period is assumed to be equal to 60 planetary rotations, resulting in a total of $M = 3000$ measurements. This case may be representative of an Earth-like planet in a WHZ of K-M dwarfs. As two relevant examples, we carry out inversions for a planet with the terrestrial topography visible either from the North or South poles: models EN3000 and ES3000. Here we used the albedo map for March 2003, which shows some snow fields on the northernmost landmasses and large areas of green vegetation.

The inversion results for these models are shown in Figs. 5 and 6, respectively. They successfully recover about 90% of the continental land mass with $A > 0.1$ and the relative standard deviation of 10–15%. The shape of the continents and their large-scale albedo features (subcontinents) are resolved on the scale of Australia and Sahara. This demonstrates the power of our algorithm.

To investigate the sensitivity of the inversion quality to the geometrical parameters, we have simulated a grid of models over a range of planet axial and orbital inclinations. Inversion results for these models are summarized graphically in Fig. 7. The plots show the dependence of the IQ (Eq. 6) and SD parameters on the inclination angles. Overall our inversion algorithm performs very well at a large range of inclination angles, except for their extreme values: the median values of IQ and SD are 86% and 12%, respectively. At higher planet axis inclination ($\geq 80^\circ$), it becomes more difficult to distinguish between the upper and lower planet hemispheres. A combination of low i_r with high i_o (like Uranus in the Solar system seen on a near edge-on orbit) is also not favorable for rotational surface imaging. However, if both i_r and i_o are low, rotational modulation still produces enough signal for a reasonable inversion. There is a particularly favorable combination – a “sweet spot” – where inversions are most successful due to a good variety of geometrical constraints on visibility and illumination of pixels: near $i_r = 50^\circ$ to 70° and i_o of 30° to 70° .

3.2. Seasonal Variations

When the planet rotational axis is inclined with respect to the orbital plane, like for the Earth, one can expect

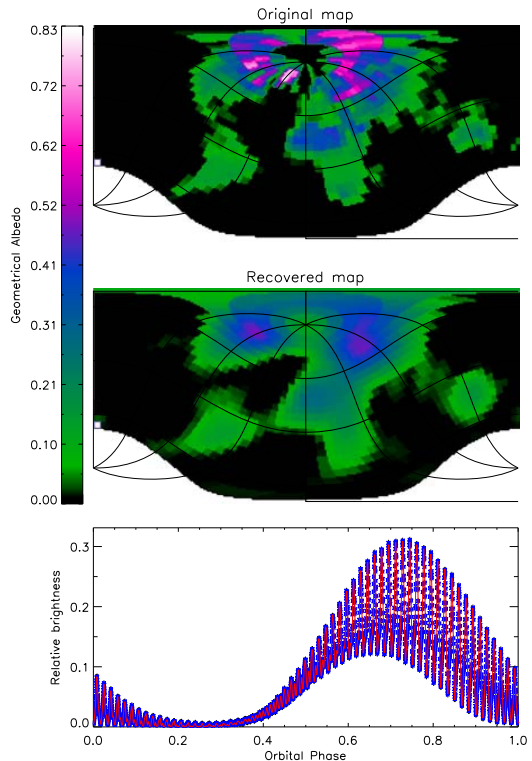


FIG. 5.— Original (top, for March 2003) and recovered albedo map (middle), and light curve (bottom) for the model EN3000 (see Table 1). The original map is used to simulate the “observed” light curve (blue symbols). The solid red line light curve is the best fit model corresponding to the recovered map. Error bars of the simulated data are smaller than the symbol size.

seasonal reflected light fluctuations due to varying snow, cloud, and biomass surface cover. In this section we analyze light curves generated from series of monthly Earth albedo maps, but yet without clouds. We consider two ways to evaluate this effect.

First, we combine 12 subsequent monthly maps (for the year 2003) and carry out inversion of a year-long light curve. Hence, seasonal variations are treated as systematic noise, and the inversion delivers an average planet albedo map. This map should be compared with the average of the 12 input maps weighted by the illumination fraction. Such weighting is necessary because the solution will be dominated by maps seen near the maximum illumination phase (i.e., near the maximum brightness of the light curve). The result for this test is shown in Fig. 8, with the same planet parameters as for the EN3000 model. As expected, the quality of the restored map is reduced because of unaccounted systematic differences in the simulated and best-fit light curves.

Second test is to use the same simulated input as in the first test but to carry out inversions on parts of the light curve. With sufficient amount of measurements, one can infer maps for different orbital phases and investigate season progression on the planet. If such variations are found, they may help to constrain the inclination of the rotational axis of the planet. The results of such tests are shown in Fig. 9. The quality is obviously reduced as compared to the EN3000 model because of the smaller amount of data. In addition, only parts of the planet surface could be inferred because of limiting illumina-

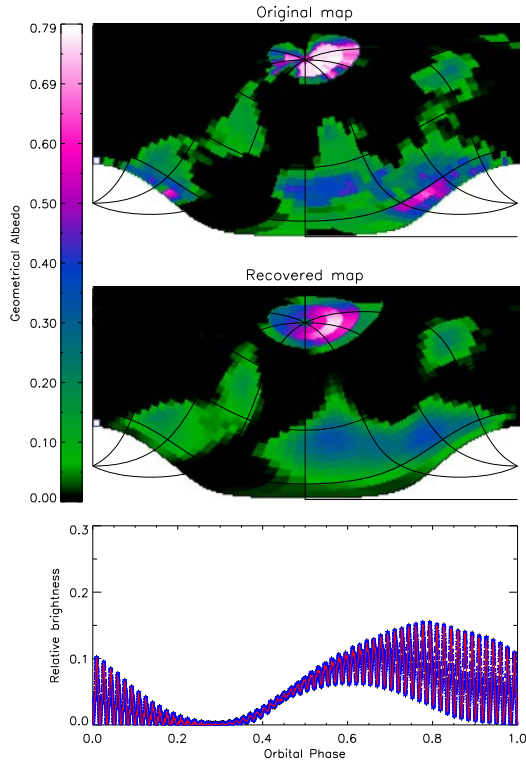


FIG. 6.— The same as in Fig. 5 for the model ES3000.

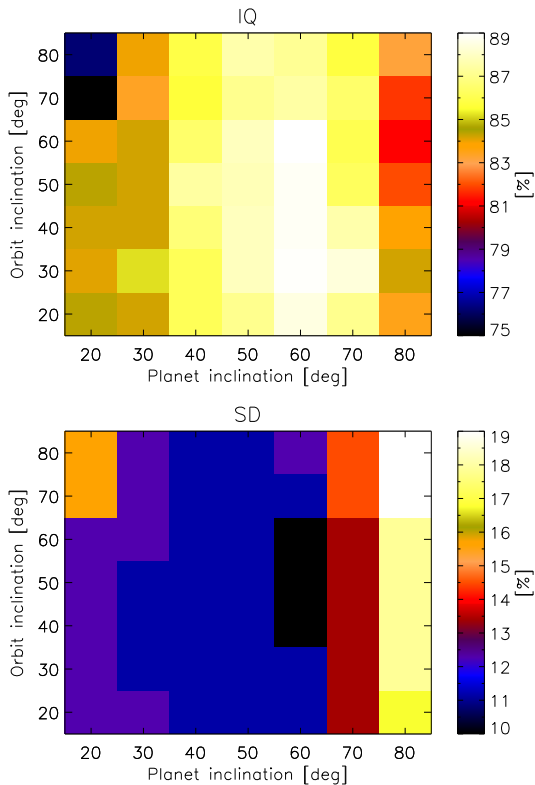
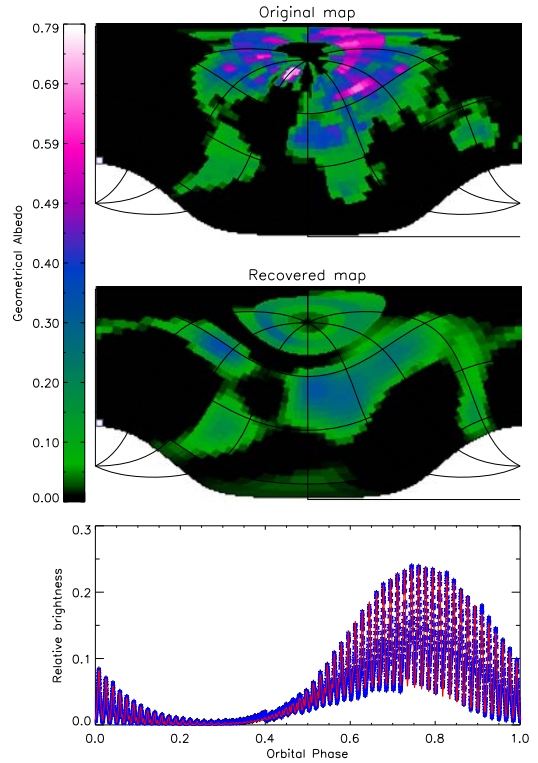

 FIG. 7.— Dependence of the IQ parameter (Eq. 6) and map standard deviation SD on the planet and orbit inclination angles i_r and i_o for the model EN3000. High values are in light tones, and low values are in dark tones. The median values of IQ and SD are 86% and 12%.


FIG. 8.— Seasonal variation effects in a year-long light curve. Top: weighted average of the 12 input albedo maps for the year 2003. Middle: recovered average albedo maps. Bottom: simulated (crosses) and best-fit (line) light curves. Error bars of the simulated data are smaller than the symbol size. IQ=84%, SD=11%.

tion at particular orbital phases. However, this exercise demonstrates that useful information on the planet surface structures can be obtained even from partial light-curve inversions.

3.3. Partially Cloudy Exo-Earths

Planets with liquid water on the surface will most probably experience a water cycle as on the Earth. This implies that clouds will be forming seasonally and sporadically, creating various weather conditions. To investigate how the information content in the recovered exoplanet albedo map depends on the cloud cover, we have computed several cases with various cloud coverages.

As in Section 3.2, we have combined 12 subsequent monthly maps for the year 2003 and augmented them with corresponding monthly cloud cover maps (also from the NEO website). The cloud maps were considered as masks with each pixel being the cloud filling factor f_c . The filling factor of the cloudless surface was correspondingly reduced by the factor $1 - f_c$. In addition, we have scaled the cloud cover by a global factor in order to quantify how optical thickness of clouds affects our ability to see the planet surface. As indicated above, the recovered map is to be compared with the average of the 12 input maps (with seasonal variations of both the surface albedo and cloud cover) weighted by the illumination fraction. Two test results are shown in Fig. 10, with the same planet parameters as for the EN3000 model and global scaling of cloud coverage by factors of 0.1 and 0.3. As expected, the quality of the restored planet surface albedo maps is significantly reduced for heavily clouded

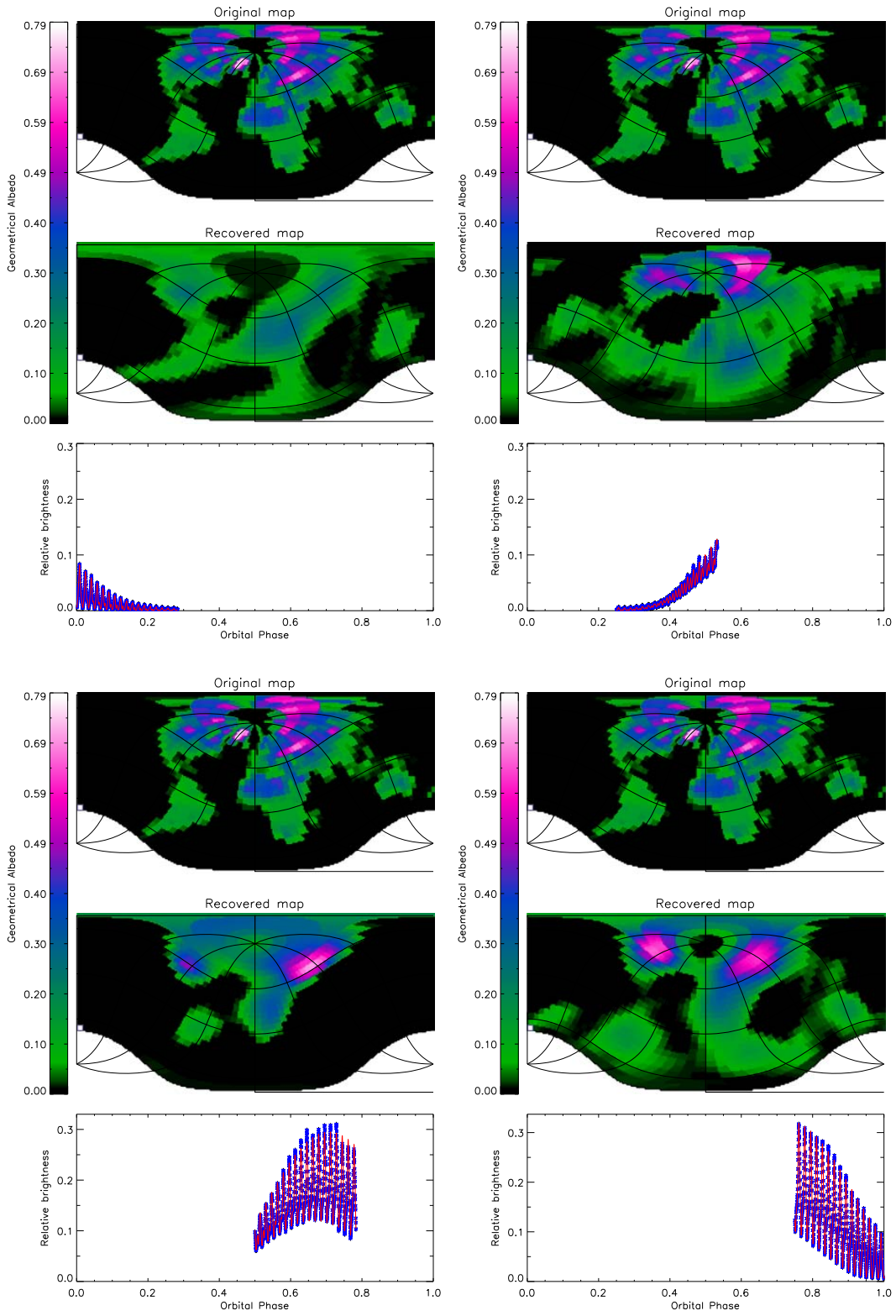


FIG. 9.— The same as Fig. 8 but for 3-month light curves. Top left: months 1-3, IQ=83%, SD=17%. Top right: months 4-6, IQ=82%, SD=12%. Bottom left: months 7-9, IQ=84%, SD=13%. Bottom right: months 10-12, IQ=89%, SD=13%.

planets. However, longer series of measurements should reveal high-contrast surface features in more detail.

If clouds dominate the planet albedo, the cloud distribution and thickness can be detected on such planets. In this case, rotational variation amplitude reduces, and the cloud light curve signal approaches that of a homogeneous sphere, as shown in Fig. 4. The recovered cloud distribution and thickness can provide additional constraints on the exoplanet climate and heat circulation in its atmosphere. The cloud physical and chemical composition can be retrieved with the help of polarization measurements as discussed in Section 3.6.

3.4. Limited Data Inversions

The inversion technique is surprisingly forgiving of S/N ratio and number of observation points. In this section, we investigate how inversions perform under less favorable conditions.

Here we compute the inversion with a reduced number of observations per planet rotation period, such as: M_{rot} is reduced to 20 and M_{ph} is reduced to 10, and vice versa, when $M_{\text{rot}}=10$ $M_{\text{ph}} = 20$. Hence, the total amount of measurements in both cases is 200, well below N (model EN200 in Table 1). The geometrical parameters are the same as before, and the orbital map is for March 2003. Despite this difference in M_{rot} and M_{ph} , these two cases result in maps of similar quality. In Fig. 11 we show one of these cases. It is only somewhat poorer as compared to the "ideal" inversion presented in Fig. 5. The major part of the landmass is recovered with realistic albedo contrast (but without some details) with IQ=87% and SD=11%. We conclude that it is the total number of measurements, not necessarily the number of measurements during a single exoplanet day that encodes the latitudinal information.

It is also interesting to see how the measurement S/N affects the output images. The case for $M_{\text{rot}} = M_{\text{ph}} = 20$ and SNR=20 is shown in Fig. 12 (model EN400 in Table 1). Here, the fraction of the recovered continent land mass is reduced to 80% and SD to 13%, and many details are missing. However, even with this low SNR, there is a high-contrast spatial structure that we could interpret as evidence of a continental water world.

3.5. Geometrical Parameter Retrieval

The light curve contains more information than just an albedo map or cloud cover. It strongly depends on the geometrical parameters of the system. Therefore, it is possible to retrieve the albedo map as well as the orbital and planetary axis angles i_o , ζ_o and i_r .

Here we retrieve these angles by carrying out inversions and minimizing the discrepancy between the "observed" and modelled light-curves within the angle domain. We have found that a high SNR light curve (100 or more) allows for a quite accurate retrieval of the angles. An example for SNR=200 is shown in Fig. 13.

Obviously, noisier data yield weaker constraints on both the albedo map and angles. For instance, for SNR < 30, even if the albedo map can be reasonably retrieved, there is simply not enough information to create a surface map without independent information about the planet geometrical parameters. In fact, both the inclination and azimuth of the orbit can be evaluated from direct imag-

ing data even in such noisier data, if the planet is well-resolved from the star. The planet's sky projected position with respect to the star changes over the course of its orbit, and the shape and orientation of this projected trajectory constrain the i_o and ζ_o angles as well as its eccentricity (astrometric orbit). When this information is employed, the retrieval procedure can successfully converge to the true planet axis inclination angle even at low SNRs. An example of such a case is shown in Fig. 14.

3.6. Polarized Reflected Light

With few assumptions the reflected planetary light will be linearly polarized, in some cases at the 10% or larger level. From Earth-like planets the light is polarized mostly due to scattering by molecules (Rayleigh), droplets or particles (clouds) in their atmospheres or reflection from the land or ocean surface (Coffeen 1979). In contrast, the direct stellar light, instrument and seeing-scattered starlight will have a much smaller linear polarization than the angularly resolved exoplanet – in many cases smaller than 10^{-5} . We will consider linearly polarized light-curve inversions in detail in a future paper, but suffice it here to note that there is considerably more information in the polarized exoplanet light-curves.

For example, the Stokes Q and U linearly polarized exoplanet light are sensitive to orbital parameters (Fluri & Berdyugina 2010), but eliminate the residual scattered starlight that generally contaminates the exoplanet photometry. Illumination variation due to, for example, elliptical orbits can also be accounted for in polarization inversion. Also, the mean component of the exoplanet rotationally modulated light polarization direction can provide the exoplanet's rotation axis inclination geometry independent of details of the surface albedo map.

More interestingly, the exoplanet scattered light polarization angle is sensitive to the exoplanetary scatterer's latitude and longitude, in a way that is completely independent from the corresponding unpolarized flux. This provides an additional constraint on the albedo map that is distinct from the seasonal and diurnal brightness variations.

Finally, reflection from the surface introduces polarized spectral features which can help to identify surface composition (Bréon et al. 2002) and biosignatures (Berdyugina et al. 2016). To distinguish true surface features from those of clouds, one has to use polarimetry simultaneously with flux measurements. In this case, it is possible to determine the scattering phase function, since polarization is strongly dependent on the scattering angle and properties of scatterers (cloud particles, surface fine structure, vegetation, rocks, etc.).

While leaving the subject of polarized light curve inversion for another paper, we expect that using polarized light will improve the sensitivity and allow inversion for other atmospheric and surface properties.

4. SOLAR SYSTEM ALBEDO INVERSIONS

In this section, we present inversions for some of the Solar system planets and moons as analogs of exoplanets. We demonstrate how our EPSI technique can recover global circulation cloud patterns as well as solid surface features without a surrounding low-albedo ocean.

For our tests we employ high-resolution composite "photographs" of planets and moons delivered by var-

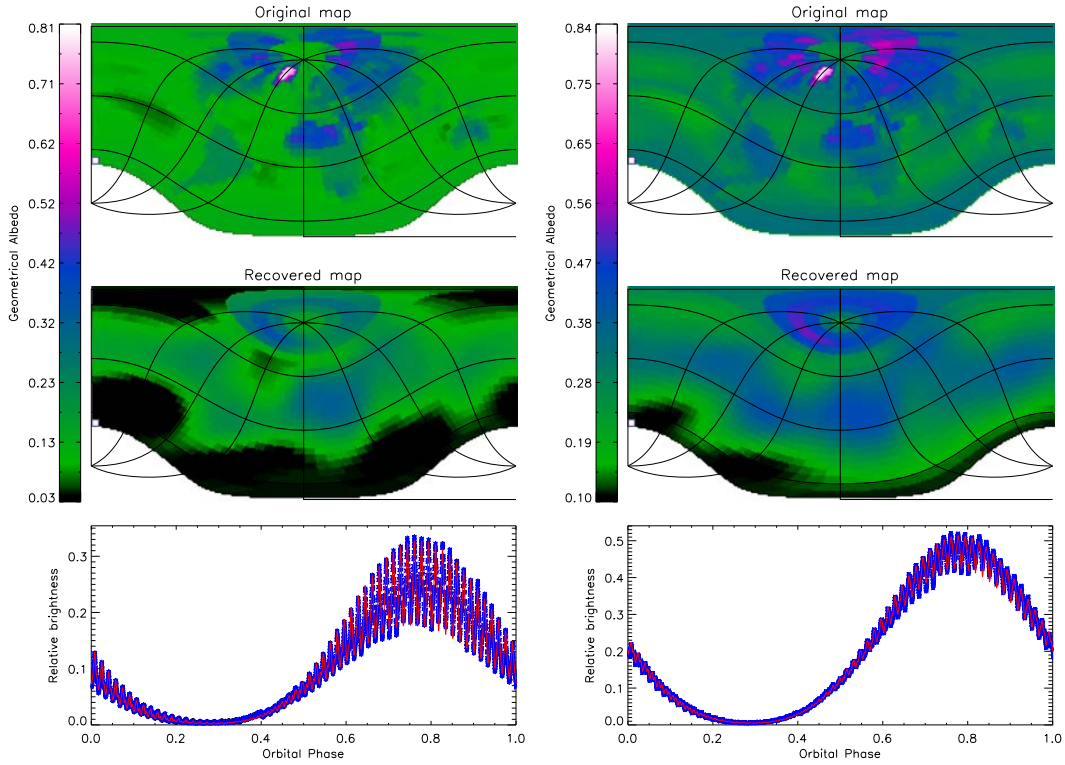


FIG. 10.— The same as Fig. 8 but for the input maps including contributions from monthly cloud coverage maps. The global cloud cover has been reduced (as compared to the measurements on the Earth) by the factor 0.1 (left, IQ=74%, SD=10%) and 0.3 (right, IQ=78%, SD=13%).

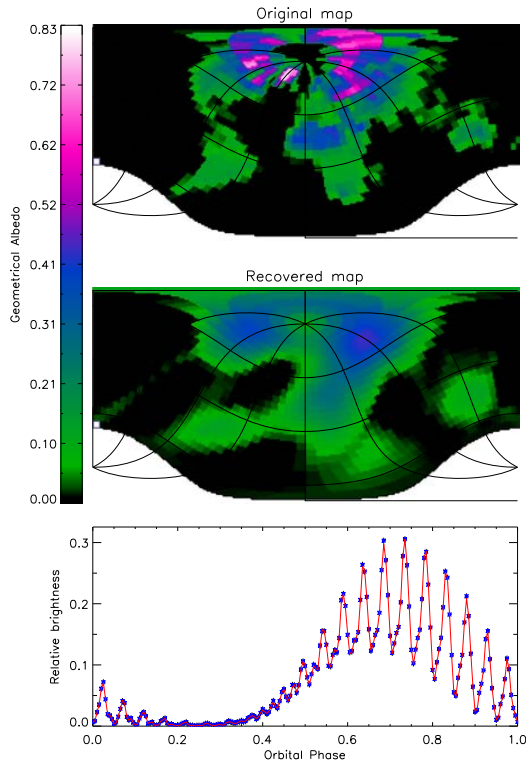


FIG. 11.— The same as in Fig. 5 but for the model EN200: $M_{\text{rot}} = 10$, $M_{\text{ph}} = 20$, SNR=200, IQ=87%, SD=11%.

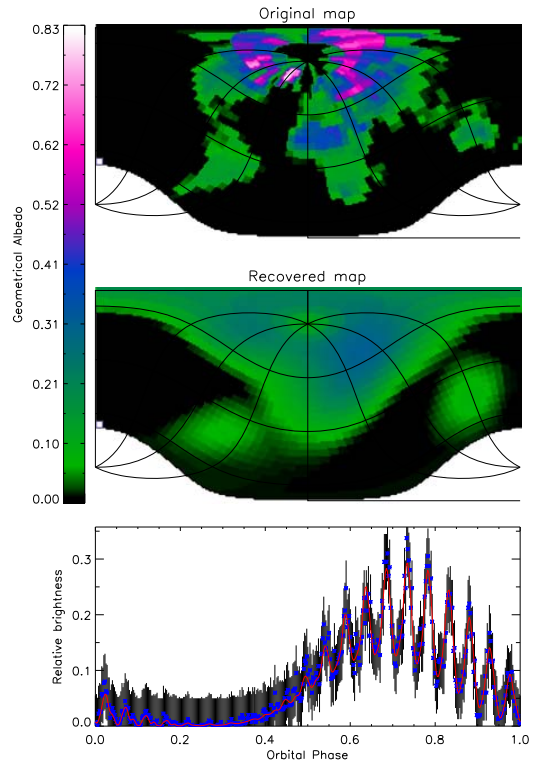


FIG. 12.— The same as in Fig. 5 but for the model EN400: $M_{\text{rot}} = M_{\text{ph}} = 20$, SNR=20, IQ=80%, SD=13%. Error bars of the simulated data are shown with vertical lines.

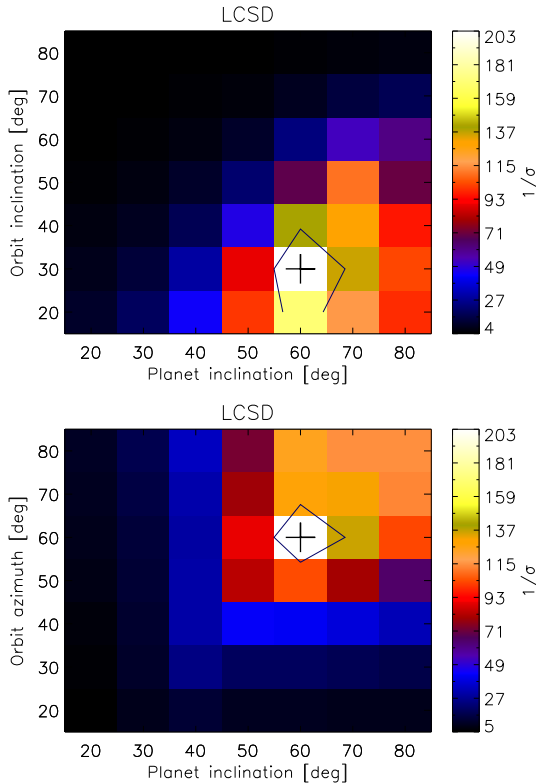


FIG. 13.— Retrievals of the angles i_o and i_r for the model EN3000 (SNR=200) by minimizing the discrepancy between the “observed” and modelled light-curves within the angle domain. The plots show inverse of light-curve standard deviations (LCSD). True values of the angles are marked with crosses. Contours show 67% confidence levels.

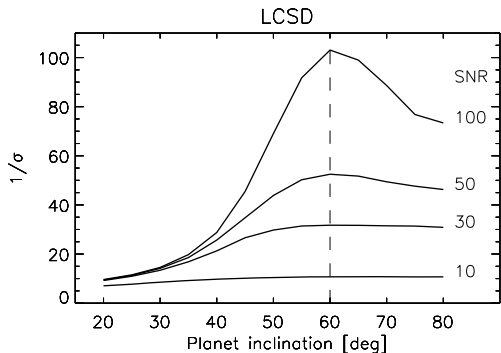


FIG. 14.— Retrievals of i_o only for the model EN3000 with SNR=10–100. The vertical axis shows inverse of light-curve standard deviations (LCSD). The true value is marked with a dashed vertical line.

ious space missions and telescopes. From each such a true-color image we extract three images for red, green and blue (RGB) bands. These images are normalized to the planet average visible geometrical albedo. Then, corresponding RGB light-curves are simulated and inverted. A composite image constructed from RGB recovered maps allows then for studying chemical composition of spatially resolved surface features by means of low-resolution spectral analysis.

Our inversions in this section assume $M_{\text{rot}} = 60$, $M_{\text{ph}} = 50$, SNR=200, $i_r = 60^\circ$, $i_o = 30^\circ$, and $\zeta_o = 60^\circ$. Only for Jupiter we assume $i_r = 30^\circ$, so that its famous

red spot is better visible.

4.1. Planets with Thick Clouds

Dense planetary atmospheres have vigorous circulation imprinted in their cloud pattern, like in zones, belts, vortices, jets, etc., on Jupiter, Saturn, Venus, etc. 3D models predict similar patterns to exist on exoplanets too (e.g., Heng & Showman 2015; Amundsen et al. 2016; Komacek & Showman 2016). Hence, images of Solar system planets with clouds can be used as a good example for testing our inversion technique to map the albedo of planetary atmospheres with a thick cloud deck. In this section, we employ images of Jupiter, Neptune, and Venus for such tests. The original and recovered images for cloudy planets are shown in Fig. 15. The details for each planet are presented in the following subsections.

We note that particles in dense clouds are usually larger than the wavelength of the optical light. Therefore, the Rayleigh approximation is not useful, and the Mie approximation is applicable only for spherical particles. In gas giants, such as Jupiter and Neptune, particles are generally nonspherical (ices) and require complicated phase functions. Therefore, the shape of their light curves is also affected by phase functions (e.g., Dyudina et al. 2016). In this section, for simplicity, when generating flux light curves from cloudy Solar system planets and applying inversions to them, we assume that clouds scatter isotropically with their geometrical albedo to be recovered by the inversion routine at different wavelengths. Thus, our first goal is to investigate how precisely low-contrast cloud structures can be recovered by the EPSI technique.

4.1.1. Jupiter

For Jupiter, we employ a global, high-resolution RGB map constructed using the *Hubble* telescope as a part of the OPAL project (Simon et al. 2015). We have extracted from this image a part with bright zones and the Great Red Spot (GRS) within the latitudes of $\pm 60^\circ$ and longitudes of $\pm 90^\circ$. Then, a full surface map from this part was constructed by rebinning it to the $6^\circ \times 6^\circ$ grid for all longitudes and latitudes. The Jupiter average visible geometrical albedo of 0.52. Correspondingly, after normalization, the average albedos of the individual RGB images are about 0.6, 0.5 and 0.4, respectively. These are close to measured values for Jupiter (Karkoschka 1994).

We have used this reduced, normalized, and rebinned RGB image for our inversions as an example of exoplanets with a global circulation cloud pattern. Also, we made it visible from the south pole, so that the GRS is well seen at higher latitudes. The GRS is well recovered as well as the zones (bright clouds) and belts (dark clouds), see Fig. 15. The overall result is very encouraging, since we can study directly hydrodynamics of thick atmospheres for angularly resolved Jupiter-like gas giants already now, with existing telescopes (see Section 7).

4.1.2. Neptune

We employ the RGB Neptune map obtained with the NASA *Voyager* mission, which discovered the Great Dark Spot (GDS) and traces of clouds at different heights in a highly windy atmosphere. Such spots (vortices) are long-lived but still transient features in the Neptune atmosphere. As for Jupiter, we used a part of the map with

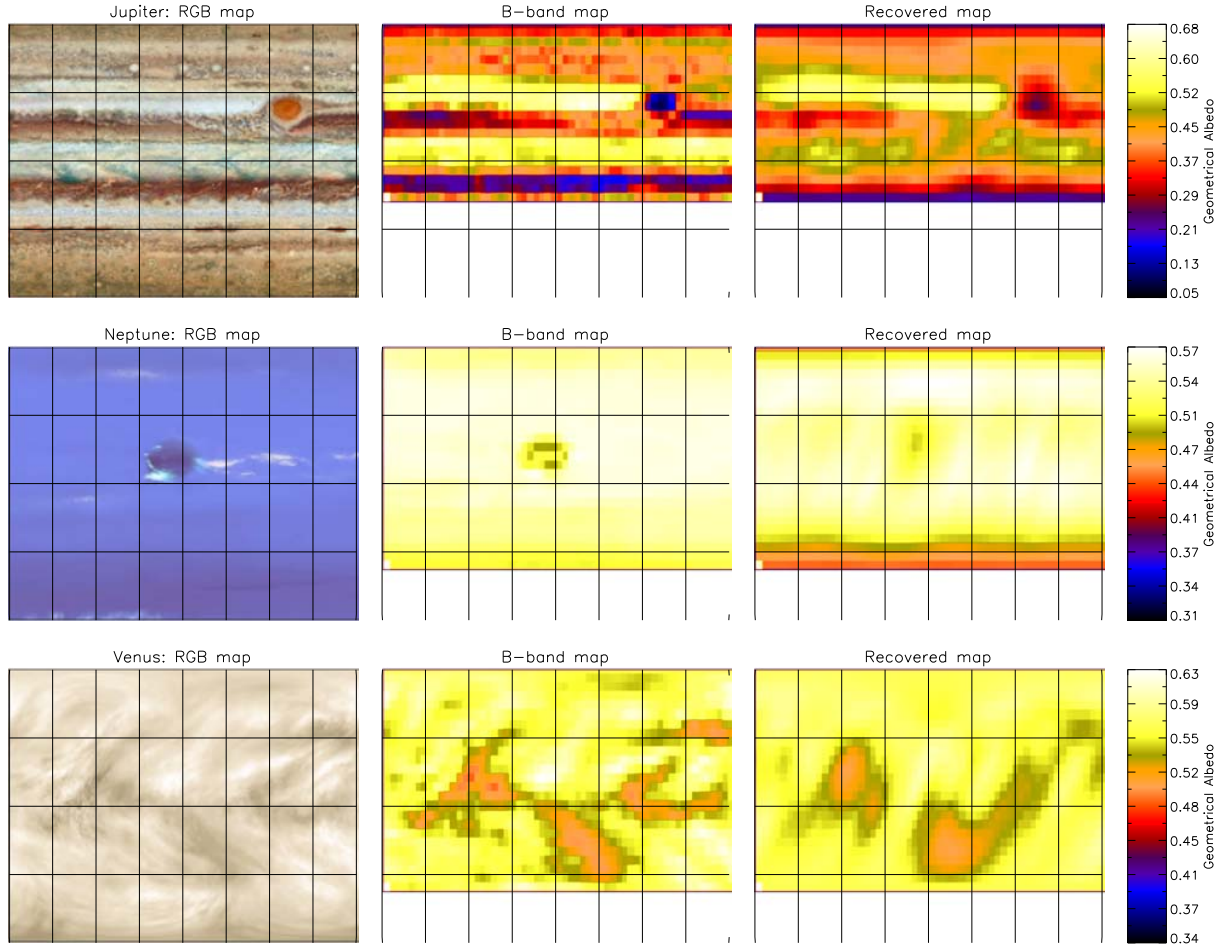


FIG. 15.— Albedo maps for the Solar system planets with thick clouds. In the first column, are original RGB maps of higher resolution, in the second column are original maps rebinned to the $6^\circ \times 6^\circ$ grid in a particular band, and in the third column are recovered maps in the same band. The assumed geometrical parameter values are $i_r = 60^\circ$, $i_o = 30^\circ$, and $\zeta_o = 30^\circ$, except for Jupiter $i_r = 30^\circ$. The original rebinned maps are used to simulate the "observed" light curve from which recovered images are obtained using inversions.

the GDS at a visible latitude. The optical geometrical albedo of Neptune is 0.41, but it is much brighter in the blue because of Rayleigh scattering and strong methane absorption in the red wavelengths.

The GDS is well recovered but traces of clouds are below the reconstruction resolution (Fig. 15). This example illustrates that blue planets may have transient vortices, which are detectable in a blue passband.

4.1.3. Venus Clouds

Venus is a cloud-enshrouded rocky planet, with clouds made of sulfuric acid droplets. It is possible that quite a few rocky exoplanets at closer distances than the inner edge of the WHZ are completely covered by clouds as Venus, with a strong green-house effect. Venus upper clouds have a transient structure driven by fast winds (jets) in its atmosphere, so the entire atmosphere rotates in only four Earth days and in the opposite direction, as compared to the 243 Earth day surface rotation. We employed the RGB image of the Venus upper clouds obtained by the NASA *Galileo* spacecraft.

The Venus cloud optical geometrical albedo is very high, 0.69. The cloud structure on Venus is different from that on Jupiter, Neptune and other gas giants (Fig. 15). It is encouraging that our indirect imaging can distin-

guish between different cloud structures and provide insights into global circulation of atmospheres on rocky and gas giant planets.

4.2. Solid Surfaces of Planets and Moons

For planets with transparent atmospheres or without atmospheres at all we can recover images of their surface albedo variations, as we demonstrated above for the Earth. Here we look at several Solar system planets and moons with interesting surface features. They generally reveal history of meteoroid bombardment and geological (tectonic or volcanic) activity. Our results are compiled in Fig. 16, and details for each planet are presented in following subsections. The Solar system moons are used here only to illustrate how an exoplanet with similar surface features can be studied (detecting and imaging an exoplanet moon would generally require much larger telescopes).

4.2.1. Mars

Mars can be considered as an analog of cold rocky planets beyond the stellar WHZ. It has seasons, polar ice caps and a very thin, transparent atmosphere, allowing a clear view of the planet surface in the optical. On the surface there are volcanoes, canyons, and traces

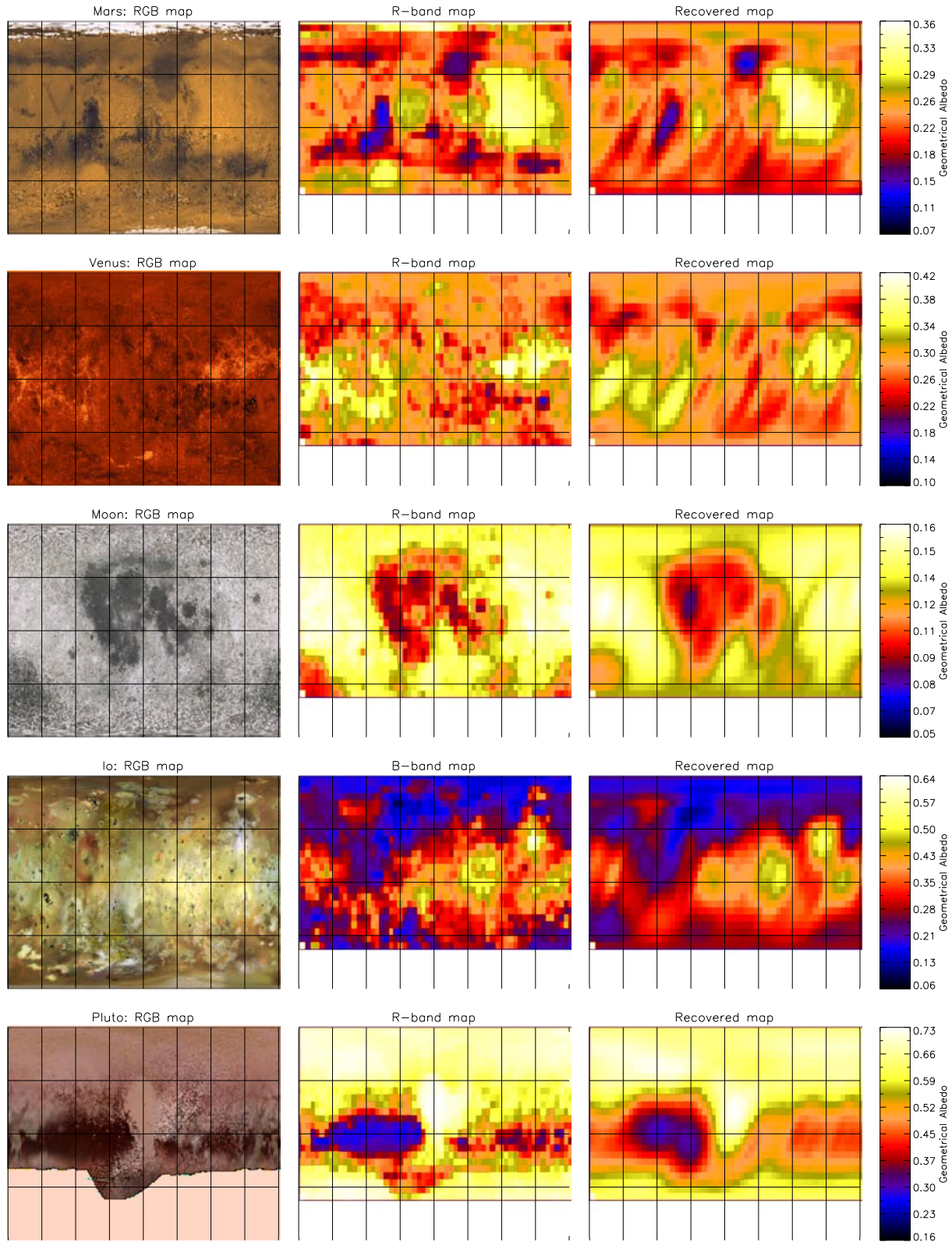


FIG. 16.— Albedo maps for surfaces of some Solar system planets and moons. In the first column, are original RGB maps of higher resolution, in the second column are original maps rebinned to the $6^\circ \times 6^\circ$ grid in a particular band, and in the third column are recovered maps in the same band. The assumed geometrical parameter values are $i_r = 60^\circ$, $i_o = 30^\circ$, and $\zeta_o = 30^\circ$. The original rebinned maps are used to simulate the "observed" light curve from which recovered images are obtained using inversions.

of earlier floods. The polar ice caps vary with seasons. The optical geometrical albedo is quite low, 0.17. We employed an RGB map of Mars obtained by the NASA *Viking* missions. When rebinned to the $6^\circ \times 6^\circ$ grid, it still shows well the largest volcano in the solar system, *Olympus Mons*, as well as a large equatorial canyon system, *Valles Marineris*.

Shapes of dark dusty areas and bright highlands, including *Olympus Mons*, are well-recovered in the R-band image. If the top of *Olympus Mons* was covered by snow, it would be quite conspicuous (see, for example a reconstruction of volcanos on Io in Section 4.2.4). Thus, seasonal variations of the albedo on exoplanets like Mars can be studied with the EPSI.

4.2.2. Venus Surface

The Venus surface is not visible in the optical because of thick clouds. Its map is obtained using radar measurements. Under the clouds, the surface looks orange because red light passes through the atmosphere. The surface is hot, and structures are relatively small-scale because of regular resurfacing. Features include craters from large meteoroids, because only those can reach and impact the surface, multiple volcanos, and some highlands. For our reconstruction we have assumed that the surface optical albedo is the same as for Mercury, 0.14, and that the surface can be seen through a transparent atmosphere.

Variations of the albedo of different structures are quite well reconstructed, including large-scale dark and bright areas with some substructures. Volcanos are quite small and are not resolved in the recovered image. However, if volcanic activity affected a larger area, that could be recovered (like on the Moon or Io, see the next section). Thus, time series of such indirect images of active exoplanets will allow studying volcanic activity and chemical composition of the new lava through multi-band spectral imaging, as discussed for biosignatures and technisignatures in Section 5.

4.2.3. Moon

The Moon is an interesting analog of an exoplanet without an atmosphere. It is highly cratered, similar to Mercury, but it also has large areas of lighter highlands and darker maria filled with volcanic lava some billions years ago. The light and dark areas have different composition. The optical albedo of the Moon is 0.12, similar to that of Mercury.

The overall shapes of the large-scale brighter and darker areas are well reconstructed. Such variety of the albedo on exoplanets without an atmosphere may help reveal the history of their formation and volcanic activity, as well as the composition of various areas.

4.2.4. Io

The Jupiter moon Io can be an analog of a very volcanically active exoplanet. Volcanic lava fills in impact craters and spreads over the surface, which is constantly renewed. Vivid surface colors of Io revealed by the NASA *Galileo* and *Voyager* missions are caused by silicates and various sulfurous compounds. In particular, volcanic plum deposits can be white, due to sulfur dioxide frost, or red, due to molecular sulfur.

We have employed a detailed RGB map of Io obtained by the *Galileo* mission. We made it visible from the South pole of the moon, so that interesting surface features are in the view. The optical geometrical albedo used is 0.45. Large-scale, active volcanic areas are well reconstructed. In particular, the volcano *Pele* distinguished by a large circular red plum deposit (in the upper left part of the map) is well seen in the recovered image. Bright volcanic slopes covered by sulfur dioxide frost, such as *Tarsus R.* (in the upper right part of the map), are also well recovered. We did not attempt it, but it seems possible that large volcanic plums forming umbrella-shaped clouds of volcanic gases can also be detected with our imaging technique, if they last long enough.

Discovering and imaging such geologically active exoplanets will be valuable for studying their internal composition. Complementary images in the infrared will help to determine temperature and age of volcanic deposits.

4.2.5. Pluto

Pluto is an icy, rocky dwarf planet which may serve as an analog of exoplanets and planetesimals beyond the so-called frost line distance from the host star. Images of the Pluto delivered by the NASA *New Horizons* mission reveal spectacular glaciers of frozen methane, carbon monoxide, and nitrogen. Extended dark surface features are possibly due to tholins (Sagan & Khare 1979), which are common on surfaces of icy outer Solar system bodies and formed by UV or energetic particle irradiation of a mixture of nitrogen and methane. The optical geometrical albedo used is 0.49. The surface of Pluto was found to have unexpected tectonic activity indicated by large craters with degradation and infill by cryomagma.

Since the *New Horizons* map of Pluto is incomplete, we assigned to the missing part a constant intermediate value albedo. Also, we made the planet visible from the pole with a detailed map, so that the missing part is basically invisible with a given inclination angle. All large-scale structures, including the brightest glacier and tholin-rich areas are well reconstructed. This is promising for detecting and studying cryovolcanic activity on icy exoplanets.

5. BIOSIGNATURES AND TECHNOSIGNATURES

In this section, we present models for spectral (broad-band) imaging of exoplanets, with the same parameters as in Section 4. We demonstrate that, for example, photosynthetic biosignatures and inorganic surface composition can be detected using EPSI. We also model hypothetical planets with global artificial structures which can be detected under certain circumstances.

5.1. Spectral Imaging of Biosignatures

Detecting biosignatures on exo-Earths is an ultimate goal of modern exoplanet studies. In most cases, this requires an analysis of the spectral content of the reflected, emitted or/and absorbed flux from an exoplanet. For example, detecting spectral signatures of biogenic (or simply out-of-equilibrium) gases in exoplanetary atmospheres is a promising approach (e.g., Grenfell et al. 2013). Positive atmospheric detections will help select promising candidates, but definite conclusions for exolife detection will require complementary studies to exclude false-positives.

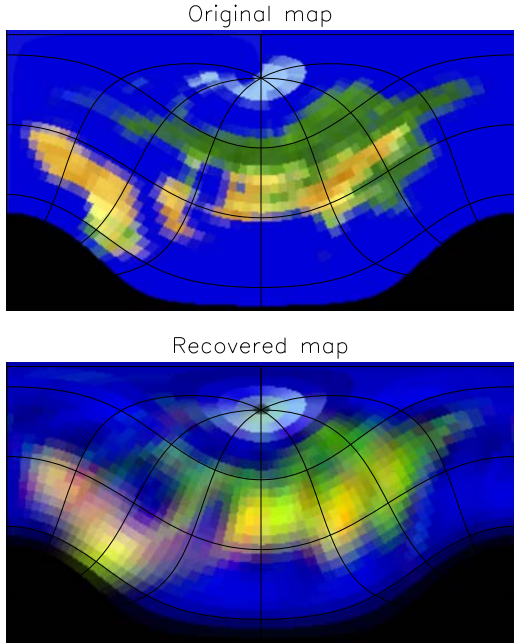


FIG. 17.— The RGB composite original and recovered maps of an exo-Earth with continents, ocean and a polar cap. Continents are in part covered by green photosynthetic organisms and in part by deserts.

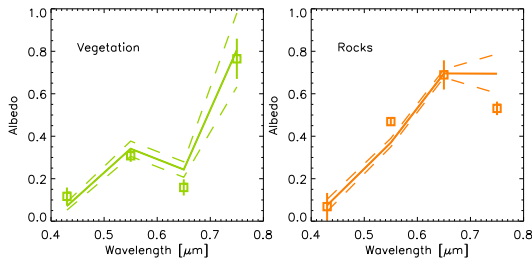


FIG. 18.— Average spectra of selected areas from the images in Fig.17. Left: spectra of a small green area at mid latitudes in the eastern part of the planet image. Right: spectra of a small desert area at lower latitudes in the western part of the planet image. Solid lines are the original image spectra. Dashed lines show a range of “natural” variations within the area in the original image. Symbols depict spectra from the recovered image. The presence of chlorophyll-rich organisms is unambiguously detected. The composition of the desert surface can be recovered by a comparison with spectra of minerals.

Here we propose such a complementary approach using our surface imaging technique applied to exoplanet light curves measured in several spectral bands or using an efficient spectrograph. We show in this Section that a “true”-color map of exoplanets inferred with our surface imaging technique could provide a powerful tool for detecting surface-based living organisms, in particular photosynthetic organisms which have dominated the Earth for billions of years.

We test our approach using a composite RGB image of Earth’s surface samples: ice polar caps, ocean reflecting blue sky, deserts, and forest. This image is shown in Fig. 17 (top panel). We complement this RGB image with a near-infrared (NIR) image (0.75–0.85 μm) using our laboratory study of various organic and inorganic samples (Berdyugina et al. 2016). In particular, the most striking feature of the IR image is high reflectance by the

green vegetation.

We have carried out inversions of the four RGB+NIR images separately, and obtained recovered images as described in this paper. The input and output images are shown in Fig. 19. Under the favorable observing conditions, the quality of the recovered images is quite good. When combined in a “true”-color photograph, the recovered RGB-image outlines quite remarkably the polar ice-cap and continents with large desert and vegetation areas (see Fig. 17, lower panel).

By resolving surface features, spectra of various areas can be extracted and explored for life signatures. An example average spectrum of a small green area at mid-latitudes in the eastern part of the planet is shown in the left panel of Fig. 18, for both the input and recovered images. A geographically resolved spectrum with a deep absorption in the visible and high albedo in the NIR has been recovered very well. It reveals quite strikingly the presence of the chlorophyll-rich organisms with the distinct red-edge signature typical for green plants and cyanobacteria. Thus, using spatially resolved images of exoplanets dramatically increases our chances to detect exolife, because we can carry out a spectral analysis of areas with high concentrations of living organisms, which is necessary for unambiguous detection (see models with various biopigments in Berdyugina et al. 2016).

In the right panel of Fig. 18, we show an example spectrum of a desert area, whose composition can be recovered using spectra of various minerals.

5.2. Artificial Mega-Structures of Advanced Civilizations

The EPSI technique allows also for detecting artificial mega-structures (AMS) constructed by advanced civilizations either on the surface or in the near-space of an exoplanet. We consider AMS to be of some “recognizable” shape and/or homogeneous albedo, and most probably to be “geostationary”. We have previously described how the thermal footprint of a civilization only slightly more advanced than that of Earth’s could be detectable at IR wavelengths from its planetary rotation signature (Kuhn & Berdyugina 2015). Since advanced civilizations would depend on stellar power sources to avoid planetary warming, it is likely that the low albedo stellar energy collectors should be detectable using the mapping technique described here.

One example of such low-albedo installations is similar to our photovoltaic systems on the Earth’s surface and in space. Such structures would absorb stellar light with high efficiency in particular spectral bands. In fact, spectral signatures of such alien photovoltaics could be of similar shapes to those of various biopigments (see Fig. 18 and Berdyugina et al. (2016)), depending on the alien technology, energy needs, and the available stellar light before or after it passes through the planetary atmosphere.

Another example would be high-albedo installations, also on the surface or in the near-space, in order to redirect the incident stellar light, e.g., for heat mitigation by reflecting the light back to space. Such installations may reflect only a particular part of the spectrum, because the amount of the reflected energy can be regulated by both the size of the structure and the width of the spectral band.

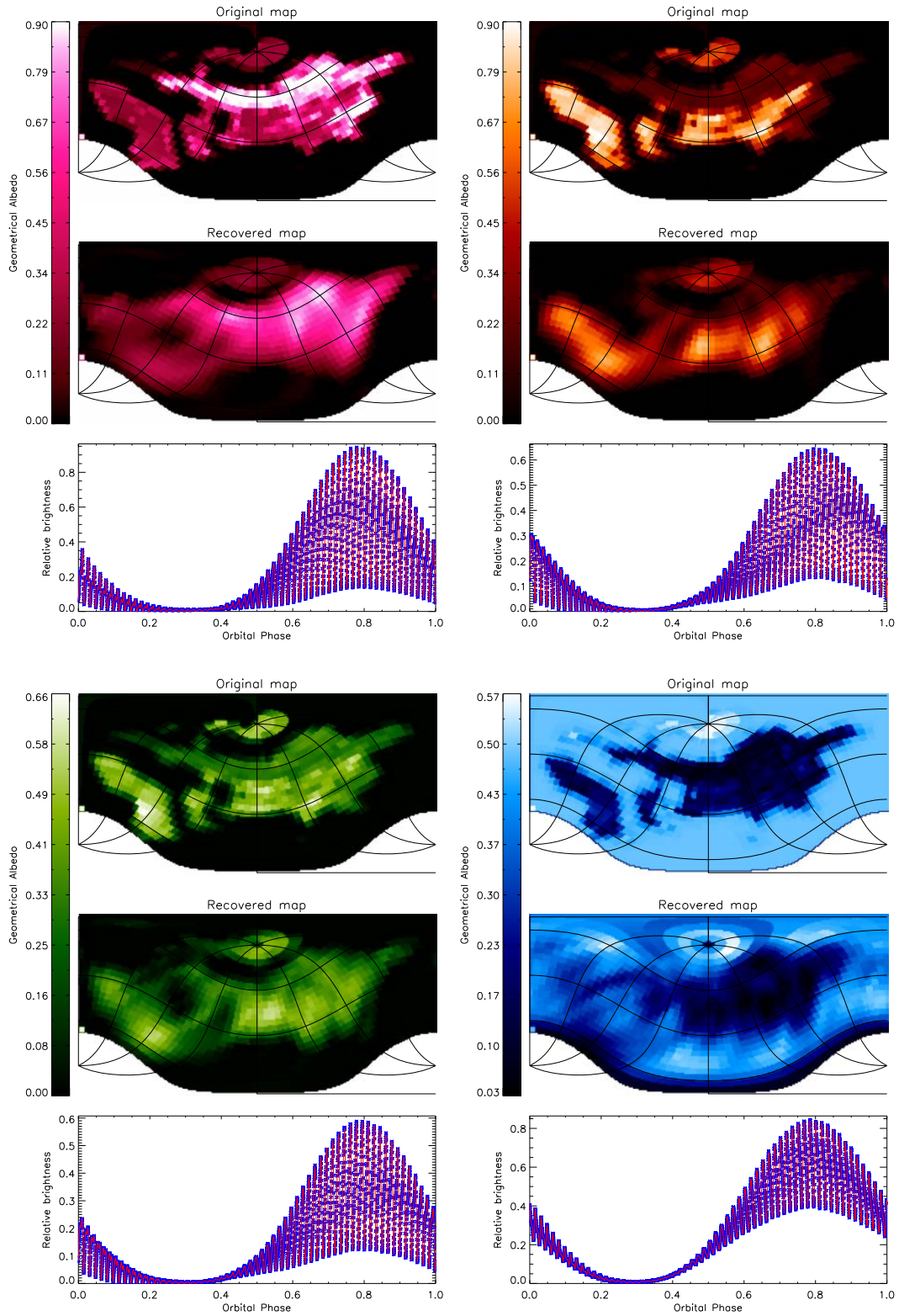


FIG. 19.— The same as Fig. 5 but for the input maps in the four RGB+NIR bands from an exo-Earth image shown in the top panel of Fig. 17. The RGB composite of the recovered images is shown in the bottom panel of Fig. 17. The map quality indexes are IR: IQ=82%, SD=16%; R: IQ=86%, SD=15%; G: IQ=88%, SD=15%; B: IQ=86%, SD=25%.

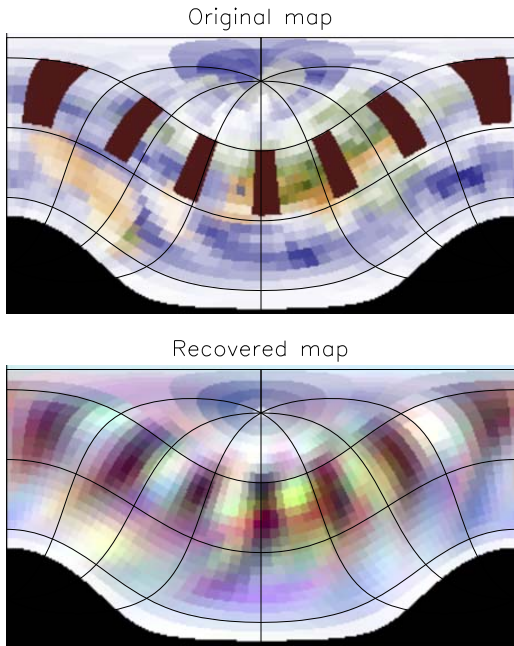


FIG. 20.— The RGB composite original and recovered maps of an exo-Earth with the artificial mega-structure of low albedo (0.05) above clouds, imitating a photovoltaic-like power-plant in space.

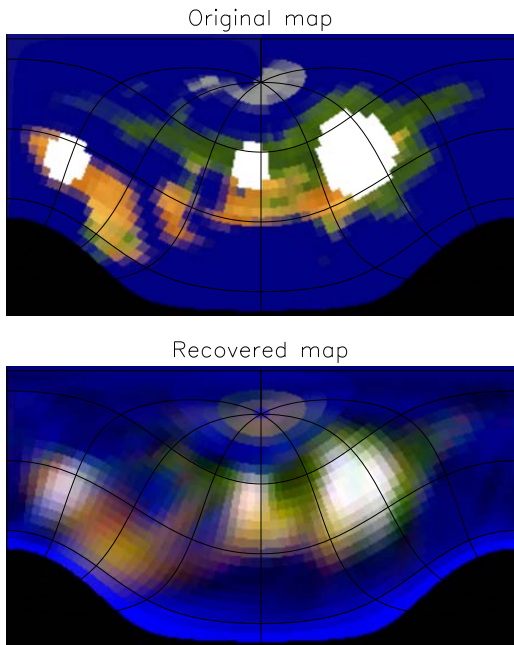


FIG. 21.— The RGB composite original and recovered maps of an exo-Earth with the artificial mega-structure of high albedo (0.9), imitating urban-like areas under reflective "umbrellas" (white circles).

We have simulated examples of exoplanets with AMS of the high and low albedo combined with natural environment, similar to the Earth. Light curves were simulated in the RGB passbands and inverted separately, as described in previous sections for natural albedo variations. The final images were obtained by combining the individual RGB light curve images into "true"-color images.

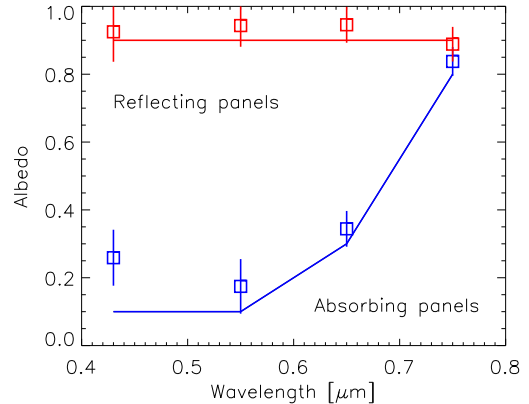


FIG. 22.— Average spectra of the artificial mega-structures shown in Figs. 20 and 21. The solid lines and symbols show original and recovered spectra, respectively. Red and blue colors stand for spectra of the high- and low-albedo, respectively.

Our model AMS are shown in Figs. 20 and 21, imitating a photovoltaic-like power-plant in space, above clouds, and urban-like areas under reflective "umbrellas" on a planet surface under a cloudless atmosphere. These numerical simulations show that recognizing AMS in inferred images requires quite large areas covered by AMS, because of uneven illumination and limited spatial resolution. Also, higher contrast structures with respect to the natural environment are obviously much more conspicuous and easier to infer than structures with the albedo similar to that of the environment.

Distinguishing such AMS from the high and low albedo natural environments (e.g., bright ice caps and mountain tops, dark lava fields and water reservoirs, etc.) may be a challenge unless they have a regular structure (like a power-plant). Also, analyzing the spectral content of the reflected light can be useful. As mentioned above, the reflectance of AMS can be limited to particular wavelengths. As examples, in Fig. 22 we show the input and recovered spectra of the AMS with absorbing and reflecting panels. The stationary nature of AMS could also be an important factor in their identification.

6. PROXIMA B AND THE ALPHA CENTAURI SYSTEM

The Alpha Centauri system stars A and B and Proxima Centauri are the closest stars to the Sun. There is at least one exoplanet discovered so far in this system – Proxima b (Anglada-Escudé et al. 2016). Gas giant, Jupiter-like planets are concluded to be incompatible with the present measurements (Endl et al. 2015). Proxima b is an excellent candidate for first-time exoplanet surface imaging.

Proxima b orbits the M5 red dwarf within its WHZ with the period of about 11.2 days at about 0.04 AU from the star. At this close distance, tidal interactions may have locked the axial rotation of the planet to its orbital period or to the 3:2 resonance as for Mercury. The presence of a dense atmosphere may influence the tidal interaction too (Kreidberg & Loeb 2016).

In this section, we present simulations and inversions for the Proxima b planet assuming tidally locked orbits at the 1:1 and 2:3 resonances. with the planetary axis inclined with respect to the orbit plane.

Since Proxima b was discovered using the radial velocity (RV) technique and so far no transits were detected,

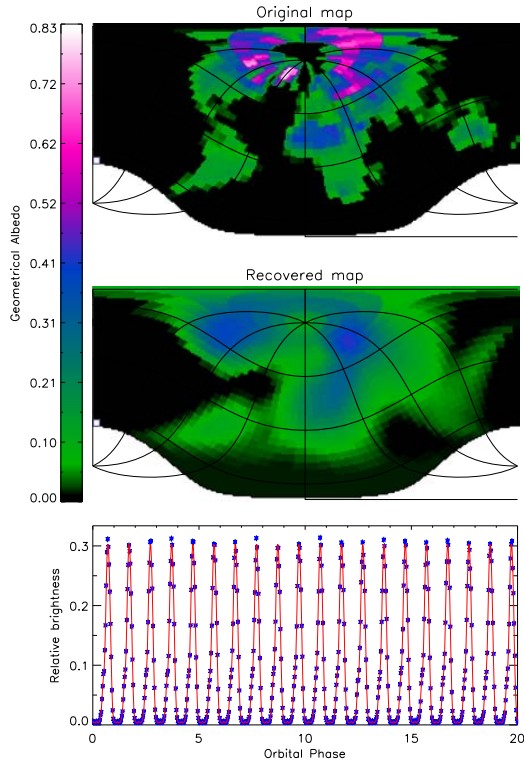


FIG. 23.— The same as in Fig. 5 for the Proxima b model with $S/N=100$ and the planet rotation being locked to the orbital motion at the 1:1 resonance. The light curves is simulated as it would be observed during several (20) orbital periods with 30 phase measurements per period, i.e., $N=600$. Here $IQ=80\%$ and $SD=13\%$.

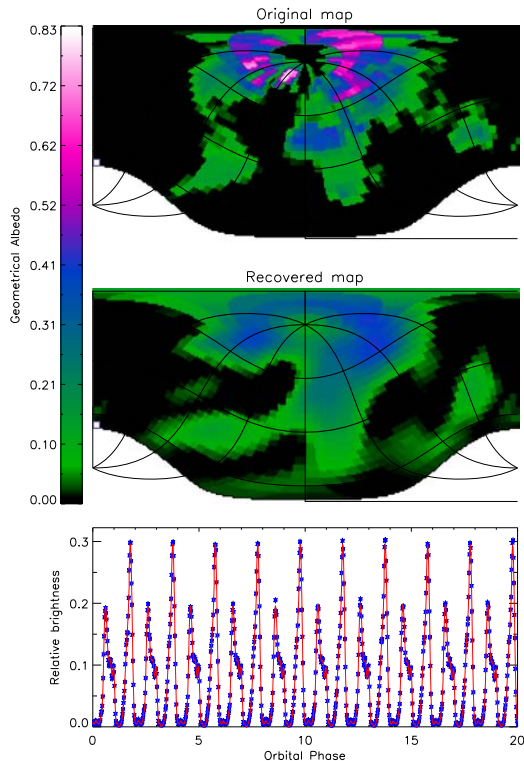


FIG. 24.— The same as in Fig. 23 for the 3:2 resonance. Here $IQ=80\%$ and $SD=13\%$.

the inclination of the orbit is still unknown. Thus, the planet can be an Earth-like planet of $1.3 - 1.5M_E$ at i_o of $90^\circ - 60^\circ$, a super-Earth of $1.6 - 5M_E$ at i_o of $55^\circ - 15^\circ$, or a Uranus/Neptune-mass planet of $15 - 17M_E$ at $i_o \approx 5^\circ$. Extremely low orbit inclinations $i_o < 5^\circ$ (a nearly face-on orbit) are still possible with a few percent chance, which may lead up to a Saturn-mass planet at $i_o \approx 1^\circ$. The composition and, hence, the surface (or cloud) albedo of such planets may differ significantly. Therefore, obtaining albedo maps (especially at different wavelengths/passbands) can provide a powerful constraint on the planet mass and composition as well as its potential habitability.

As in Section 3.1, we test our inversion technique for Proxima b parameters using cloudless Earth’s albedo maps. We assume the orbit inclination of 60° corresponding to a $1.5 M_E$ planet. With the terrestrial mean density of 5.5 g/cm^3 its radius would be $1.15 R_E$, which we use in our reflected light simulations. Here, the $SNR=100$ is assumed.

The two scenarios when the planet rotation is locked to the orbital motion at the 1:1 and 3:2 resonances are shown in Fig. 23 Fig. 24, respectively. The fact that the periods are the same or very close hinders the amount of information in the light curve, even though we allow observations during several orbital periods. However, most of the landmass (80%) is still recovered and its outline is quite recognizable. The quality of the map is higher for the 3:2 resonance orbit because there are two different light-curves observed every other orbital period. Here, the number of measurements and the SNR can be increased by observing during several orbital periods, as shown in our inversions.

Since the rotational axis inclination angle and the orbit normal azimuth are unknown, we vary them to understand imaging capabilities of this planet, possibly locked at a resonance rotation. The IQ and SD parameters of our inversions for the periods locked at 1:1 are shown in Figs. 25. Similar to the unlocked case, the most favorable planet axis inclination angles range within 30° to 60° , while the orbit normal azimuth angle can be in a wide range.

7. OBSERVATIONAL REQUIREMENTS

In this section, we investigate and formulate observational requirements for the telescope size and scattered light level, in order to obtain spectral images of Proxima b and possible rocky planets in the nearest to the Sun stellar system Alpha Centauri A and B. We also estimate how many Earth-size and super-Earth planets in WHZ can be imaged with our EPSI technique depending on the telescope aperture for a given scattered light background.

7.1. Contrast Profile

The level of the stellar scattered light, or contrast C with respect to the central star brightness, plays an important role in the planet reflected light SNR. The required SNR has to be achieved above the bright background at the WHZ angular distance from the star, where an Earth-like planet may reside. This component of the SNR budget is missing in the computations made by Fujii & Kawahara (2012) and leads to unrealistic sensitivities.

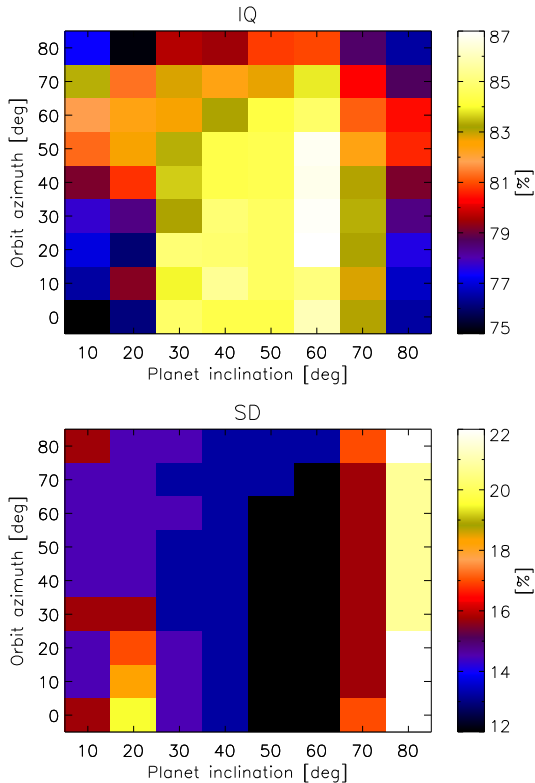


FIG. 25.— Dependence of the IQ parameter (Eq. 6) and map standard deviation SD on the planet axis inclination angles i_r and the orbit normal azimuth ζ_o for the Proxima b model with the periods locked at 1:1. High values are in light tones, and low values are in dark tones. The median values of IQ and SD are 80% and 16%.

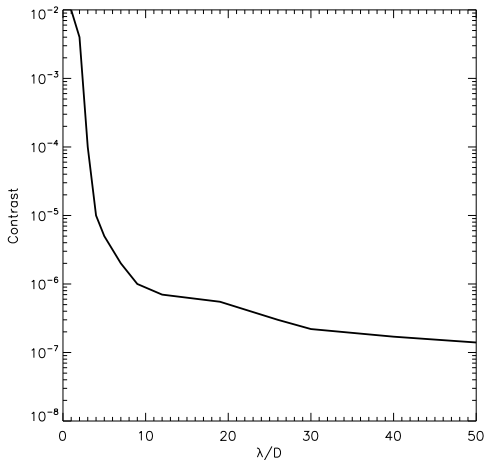


FIG. 26.— An assumed contrast curve for the scattered stellar light brightness versus the angular distance from the star in units of the ratio of the wavelength λ to the telescope diameter D (for an unsegmented mirror telescope). The contrast reaches 10^{-7} at $\lambda/D = 100$.

For reference, we take the contrast curve similar to the existing state-of-the-art performance achieved with the SPHERE imaging instrument at VLT (Langlois et al. 2014, 2017) using adaptive optics (AO), and spectral and angular differential imaging. We have also attempted to semi-quantitatively include the effects of wavefront phase errors, i.e., “speckle noise” (Aime & Soummer 2004) by

scaling this coronagraph/AO-limited curve to other telescopes. A representative contrast profile that varies with the angle θ from the central star, expressed in units of the ratio of the wavelength λ to the diameter D , is shown in Fig. 26.

We emphasize that this contrast curve is achieved for a telescope with an unsegmented primary mirror. For a highly segmented primary mirror, without heroic segmented coronagraphy and speckle nulling AO, the contrast curve suffers from scattering off the segment edges and may not reach even 10^{-5} contrast at the required angular separation.

We expect that the contrast of Keck-style telescopes (with a multi-segmented primary mirror and a single secondary mirror) will be worse than that of a unsegmented telescope by approximately a factor equal to the number of mirror segments in the full aperture. For example, we scale up the SPHERE C profile with the factors of 50, 500, and 800 to obtain rough estimates of SNR and number of detectable WHZ planets using a Keck-, TMT- and EELT-like telescopes with segmented primary mirrors.

On the other hand, recently proposed hybrid interferometric telescopes, such as the 74m Colossus or 20m ExoLife Finder (ELF), can achieve contrast performance comparable to or even better than that of single-mirror telescopes (Kuhn et al. 2014; Moretto et al. 2014), at least in selected parts of their field of view (FOV). Such an optical system consists of an array of off-axis telescopes from a common parent parabola. Each off-axis telescope consists of the active primary and adaptive secondary mirrors. They build a common focus pupil image with the angular resolution equivalent to the diameter of the telescope array. Analogous to the nulling interferometry, independent off-axis apertures can be phased to “synthesize” a PSF with a dark hole of extremely low scattered light and speckle noise. This dark hole can be moved within the FOV to follow an exoplanet orbiting the star by readjusting the aperture phases. Therefore, for simplicity, we assume here that the contrast curve shown in Fig. 26 is also valid for a Colossus/ELF-type telescope at the location of an exoplanet.

Another improvement of the telescope/coronagraph performance can be achieved by using polarimetry to enhance the contrast of polarized light reflected from a planet above the stellar background. This technique has been employed for detection and detailed studies of circumstellar disks (e.g., Kuhn et al. 2001; Oppenheimer et al. 2008; Benisty et al. 2015; Follette et al. 2017) as well as exoplanets unresolved from their stars (Berdyugina et al. 2008, 2011). The direct imaging instruments SPHERE at VLT and GPI at Gemini have this option and are successful in imaging circumstellar disks and resolved companions.

An important contribution to the SNR budget for ground-based telescopes is the brightness of the sky. We have used sky magnitudes for the dark time at the ESO Paranal Observatory, Chile, by Patat (2008), while averaging variations due to the 11-year solar cycle. We note that the sky contribution is more important for fainter stars observed with smaller telescopes. As the aperture of the telescope increases, the size of the resolution element decreases, and the sky contribution decreases as well.

Thus, we compute the number of photons from three

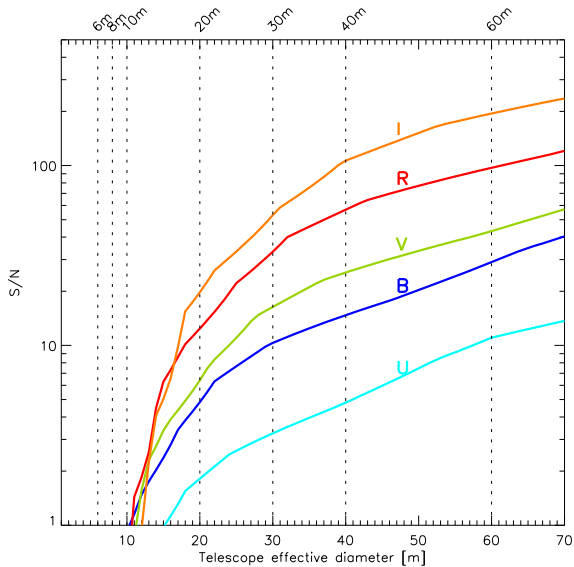


FIG. 27.— SNR curves for an Earth-like planet like Proxima b (see parameters in the text) depending on the effective telescope diameter, when assuming a single, unsegmented primary mirror. The SNR is computed for 1h exposure time in the UBVRI passbands, when only a half of the planet is illuminated. The assumed contrast curve for the stellar scattered light is shown in Fig. 26. The planet average surface albedo in all bands is assumed to be 0.2 for simplicity, which allows to scale the SNR for other albedo values. Vertical dashed lines indicate effective diameters (unsegmented) of the existing and planned telescopes. The resolving power of the telescopes is assumed defined by the effective diameter.

different sources: the planet itself, the scattered stellar background at a given angular separation from the star, and a sky background area equal to the resolution element of a given telescope aperture. In this way, in the following sections, we compute SNR for exoplanets in the standard Johnson UBVRI bands depending on the size of the telescope, using known stellar and planetary parameters.

7.2. SNR for Proxima b

Achieving SNR=100 in the reflected light from an exoplanet is rather challenging even for the nearest exoplanet, such as Proxima b. Here we compute SNR in the UBVRI passbands for 1 hr exposure time, when assuming the telescope efficiency 25%, the illumination phase of the planet 0.5 (maximum elongation from the star), and the average surface albedo in all bands 0.2. The stellar magnitudes used are from the SIMBAD database. The result is shown in Fig. 27.

Such a SNR computation produces photon-limited estimates which can be considered as some realistic upper limit values. Systematic errors are usually specific to a particular instrument design and calibration and data reduction procedures. Hence, we assume here the best case scenario, when all other errors are reduced down to the photon-noise level. In practice, to detect reflected light variability, one should also allow for smaller illumination phases (down to at least 0.1) and smaller surface albedo (down to 0.05). For example, the reflectance of vegetation in the optical is about 0.05. The reflectance of rocky terrains and deserts is between 0.1 and 0.15, and that of the ocean is 0.1 in the blue (due to sky reflection) and less than 2% in the red and NIR. The glint on the ocean

due to Fresnel sunlight reflection is very bright, but its relative contribution with respect to landmasses is low.

We also note that because of the orbit inclination to the line of sight, the star-planet projected angular separation varies with the orbital phase, leading to different C levels at different orbital phases. Hence, orbital phases near conjunctions will be hindered by higher C and, therefore, lower SNR for the same exposure time. For example, for the assumed orbit inclination of 60° for Proxima b the angular separation between the star and the planet varies by a factor of two, i.e., between 37 mas at maximum elongations and 18 mas near conjunctions. Thus, observing Proxima b near conjunction phases may require a telescope system with a larger resolving power or a better contrast at smaller θ angles, depending on the orbit inclination.

The overall conclusion from this exercise is that a telescope with low scattered light, the effective diameter $D \geq 12$ m, and an equivalent or larger angular resolving power is required for detecting an Earth-like Proxima b above the star and sky background in the BVRI bands with $\text{SNR} \geq 2$ during 1hr exposure time. A large telescope (≥ 20 m) is preferable for more efficient observations.

The BVRI band measurements are particularly interesting for detecting possible photosynthetic life signatures as described in Section 5.1 and Berdyugina et al. (2016). A 20m-class telescopes should be able to achieve SNR 5 to 20 in the BVRI-bands in 1h, at least near maximum elongations of the planet. The R-band measurements during several orbital periods with $\text{SNR}=20$ will be already usable for surface inversions. With such a dedicated telescope in Chile, Proxima b can be observed between 3 to 7 hours/night during 6 months (February to July). Even when discarding 10% observing time for bad weather condition, one can obtain about 800 1h-measurements spread over 16 orbital periods within just one season. Observing in at least three adjacent passbands simultaneously (e.g., BVR or VRI) should be possible for the successful operation of the adaptive optics system.

Hence, after only one season of observations we will be able to obtain the first "color photographs" of Proxima b. If the planet is partially cloudy, several observing seasons are needed to filter out the cloud noise and obtain more detailed surface maps. If planet is completely covered by thick clouds or its surface is completely featureless, we will be able to conclude on its bulk properties already after a few orbital periods (1–2 months).

7.3. SNR for Alpha Centauri A and B potential planets

A search for planets around the Alpha Centauri A and B components has already ruled out Jupiter-like planets in their WHZ (Endl et al. 2015), but there is still hope for smaller planets, which were not yet detected or ruled out due to sensitivity limits. If any planets in WHZ of these stars will be found, they will be excellent targets for our indirect surface imaging.

We have computed the SNR diagram for an Earth-size planet with an average geometrical albedo 0.2 and at the half illumination orbital phase within the WHZ of the Alpha Centauri A and B stars – about 930 mas and 560 mas, respectively (see Fig. 28). Resolving the WHZ of these stars is theoretically possible even with a

1m class telescope, but achieving a significantly higher contrast level is needed for detecting Earth-size planets around these more luminous stars. Hence, such planets may remain undetectable in the optical or NIR with 8–10m class telescopes, but they can be easily detected with a 20m-class telescope, assuming the contrast curve shown in Fig. 26.

Our result suggests that formally, with a longer exposure time (≥ 10 h), an Earth-like WHZ planet may be detected around Alpha Cen B with an 8m telescope at $\text{SNR}=5$. In practice, however, systematic errors accumulated over several nights may prevent achieving the photon-limited SNR. Also, if the planetary orbit is coplanar with the binary (AB) orbit, i.e., $i_o \approx 80^\circ$, such a detection is only possible at planet maximum elongations from the star. Near the "full-moon" phase the planet-star angular separation is reduced by a factor of almost 6, which leads to a severe increase of the stellar light background and makes such a planet undetectable. Considering that the orbit orientation on the sky plane is also unknown, the direct detection of an Earth-size planet in the WHZ of Alpha Cen B with an 8m-telescope may take a long time.

Similar to the Proxima b case discussed in the previous section, dedicated continuous direct imaging observations of the Alpha Centauri A and B stars with a larger telescope may reveal (or exclude) Earth-size planets in their WHZ. Obviously, larger planets can be detected within shorter observing time, as the SNR increases with the size of the planet. The advantage here is that these planets will most probably have axial rotation periods different from the orbital periods (not tidally locked), which will allow for a more detailed surface mapping as presented in Section 3.

7.4. Number of Detectable Exoplanets

Assuming the telescope and instrument performance as in Section 7.2, we can evaluate how many WHZ Earth-size planets in the solar neighbourhood can be potentially detected and surface-imaged. From the SIMBAD database, we have compiled a list of AFGKM main sequence stars brighter than $V = 13$ magnitude (about 3500 stars). We have computed their WHZ distances by scaling the Sun-Earth WHZ with the stellar luminosity for an Earth-like planet. The reflected light flux is computed using the Earth size, geometrical albedo 0.2 for all passbands, and 0.5 illumination phase. We consider a planet detectable if $\text{SNR} \geq 5$ can be achieved during 4h exposure time.

The number of Earth-size ($1 R_E$) detectable planets is plotted for different telescope sizes and types in Fig. 29. The plot shows that a 20m-class telescope with the SPHERE-like performance (like the ELF) can detect and surface image a dozen of WHZ Earth-like planets. Hundreds of such planets in this magnitude-limited sample could be detected by a 70 m telescope (like the Colossus). However, we evaluate that most probably none of such planets can be detected by Keck-style telescopes with $D < 45$ m.

The number of detectable super-Earths up to the Neptune size ($4 R_E$) is plotted for different telescope sizes and types in Fig. 29. In this case, a 20m coronagraphic telescope can detect and image hundreds of planets, while all such planets can be discovered and imaged with a 60m

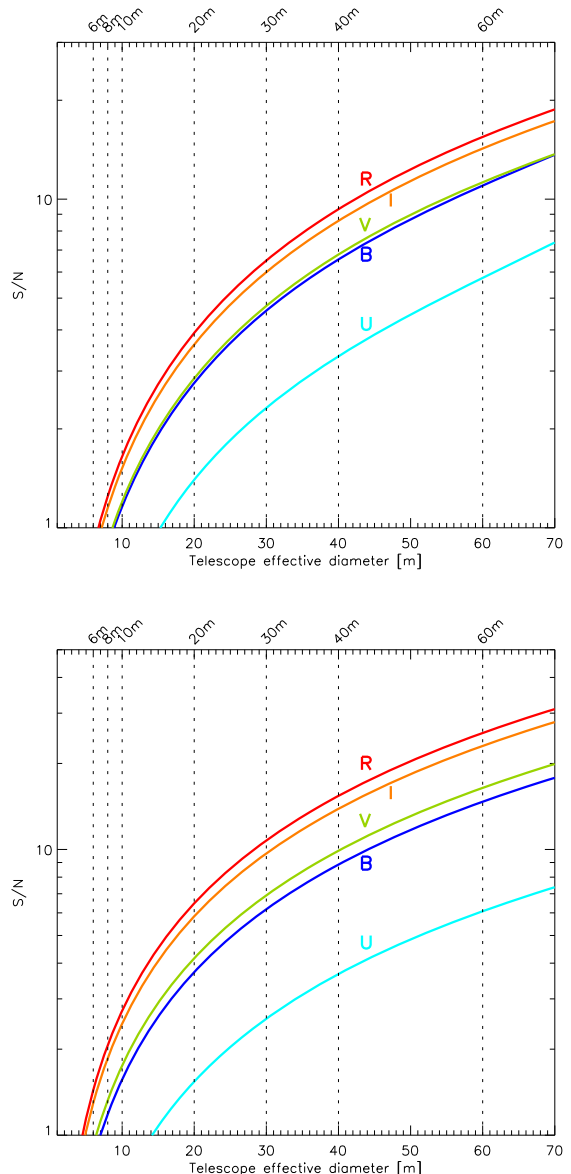


FIG. 28.— The same as Fig. 27 but for α Cen A and B (top and bottom) hypothetical Earth-size planets residing in their corresponding (liquid water) habitable zones.

high-performance telescope. Multi-segmented Keck-style telescopes, such as TMT and EELT, should be able to collect enough photons above the stellar background for tens of such planets. Jupiter-size planets are more realistic targets for such telescopes.

8. SUMMARY AND CONCLUSIONS

This paper demonstrates that for many exoplanets it is possible to map their surface or cloud structures using reflected starlight analyzed with the ExoPlanet Surface Imaging (EPSI) technique. We have shown that time resolved exoplanet photometry (on the scale of a few percent of the exoplanet rotation period) and with the SNR of as low as 20, can yield enough information to, for example, detect continents on a water-rich world. With higher SNR it may be possible to trace the outline of continents and their large-scale albedo features, such

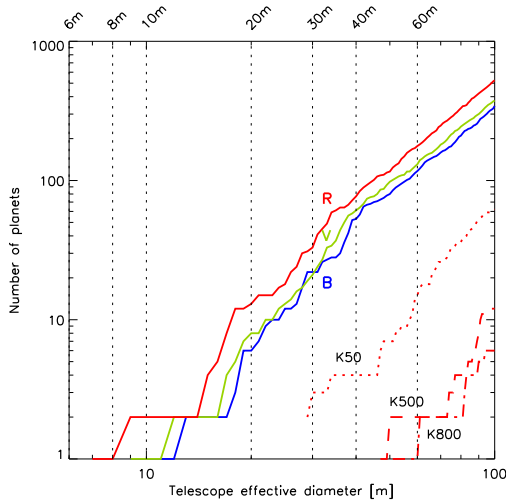


FIG. 29.— Number of detectable WHZ Earth-size planets ($1 R_E$) in the BVR bands ($\text{SNR} \geq 5$) around AFGKM main sequence stars brighter than $V = 13$ magnitude. Solid lines are for unsegmented or interferometric telescopes which can achieve the contrast as shown in Fig. 26. Dotted, dashed and dashed-dotted lines are for Keck-type telescopes (segmented primary and single secondary mirrors) with the number of segments of 50, 500, and 800, respectively. Here, the exposure time is 4h, the planet albedo is 0.2 in all bands, illumination phase is 0.5.

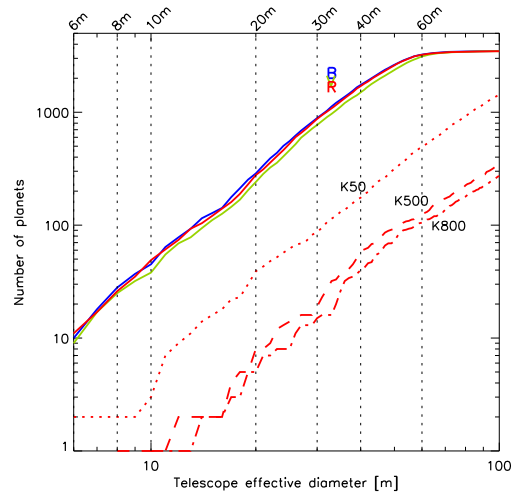


FIG. 30.— Same as Fig. 29 but for planets of $4 R_E$, which is about the size of Neptune. All such planets (and bigger ones) in the solar neighbourhood could be detected and surface imaged with a 70m Colossus-like telescope.

as deserts, vegetation areas, snowfields, icecaps, etc., or even artificial "alien megastructures."

Combining EPSI with spectrally resolved data may yield information about exoplanetary subcontinental-scale biomarkers. Planetary "noise" like clouds would limit such observations, but under some circumstances only by decreasing the surface albedo contrast.

These data are within reach of the next generation of coronagraphic telescopes. For example a dedicated hybrid telescope-interferometer of 12–20m diameter could generate surface maps in different colors for the nearest exoplanet, Proxima b, and a few others. Dozens of Earth-size exoplanets and hundreds of larger planets could be imaged this way with a hybrid telescope of 30m or larger diameter.

SVB acknowledges the support by the ERC Advanced Grant HotMol (www.hotmol.eu). JRK acknowledges the support by the Alexander von Humboldt Foundation, Germany.

REFERENCES

- Aime, C., & Soummer R., 2004, *ApJ*, 612, L85
 Amundsen, D.S., Mayne, N.J., Baraffe, I., et al. 2016, *A&A*, 595, id.A36, 11 pp.
 Anglada-Escudé, G., Amado, P.J., Barnes, J., et al. 2016, *Nature*, 536, 437
 Benisty, M., Juhasz, A., Boccaletti, A., Avenhaus, H., et al. 2015, *A&A*, 578, id. L6, 7 pp.
 Berdyugina, S. V., 1998, *A&A*, 338, 97
 Berdyugina, S. V., Berdyugin, A. V., Ilyin, I., Tuominen, I., 1998, *A&A*, 340, 437
 Berdyugina, S. V., Pelt, J., Tuominen, I., 2002, *A&A*, 394, 505
 Berdyugina, S.V., Berdyugin, A.V., Fluri, D.M., & Pirola, V. 2008, *ApJ*, 673, L83
 Berdyugina, S.V., Berdyugin, A.V., Fluri, D.M., & Pirola, V. 2011, *ApJ*, 728, L6
 Berdyugina, S.V., Kuhn, J.R., Harrington, D.M., Santl-Temkiv, T., Messersmith, E.J. 2016, *International Journal of Astrobiology*, 15, 45
 Berdyugina, S.V. 2016, in *Radiation mechanisms of astrophysical objects: classics today*, eds. V.P. Grinin, H. Harutyunian, V.B. Il'in, A.F. Kholtygin, A. Nikoghossian, Edit Print Publ. House, p. 151 (arXiv:1607.06874)
 Bréon, F.M., Buriez, J.C., Couvert, P., et al. 2002, *Adv. Space Res.*, 30, 2383
 Coffeen, D.L. 1979, *JOSA*, 69, 1051
 Cowan, N.B., Agol, E. 2008, *ApJ*, 678, L129
 Cowan, N.B., Agol, E., Meadows, V.S., et al. 2009, *ApJ*, 700, 915
 Crossfield, I.J.M., Hansen, B.M.S., Harrington, J., et al. 2010, *ApJ*, 723, 1436
 Demory, B.-O., Seager, S., Madhusudhan, N., et al. 2011, *ApJ*, 735, L12
 Dyudina, U., Zhang, X., Li, L., et al. 2016, *ApJ*, 822, id. 76, 10 pp.
 Endl, M., Bergmann, Ch., Hearnshaw, J., et al. 2015, *Int. J. Astrobiology*, 14, 305
 Evans, T.M., Pont, F., Sing, D.K., et al. 2013, *ApJ*, 772, L16
 Faigler, S., Mazeh, T. 2015, *ApJ*, 800, id. 73, 10 pp.
 Fluri, D.M., & Berdyugina, S.V. 2010, *A&A*, 512, id.A59, 12 pp.
 Follette, K.B., Rameau, J., Dong, R., et al. 2017, *AJ*, 153, id. 264, 15 pp.
 Fujii, Y., & Kawahara, H., 2012, *ApJ*, 755, id. 101, 14pp.
 Grenfell, J.L., Gebauer, S., Godolt, M., Palczynski, K., Rauer, H., Stock, J., von Paris, P., Lehmann, R., Selsis, F. 2013, *Astrobiology*, 13, 415
 Hansen, J.E., & Travis, L.D., 1974, *Space Sci. Rev.*, 16, 527

- Harrington, J. Hansen, B.M., Luszcz, S.H., et al. 2006, *Science*, 314, 623
- Heng, K., & Showman, A.P. 2015, *Ann. Rev. Earth & Planet. Sci.*, 43, 509
- Karkoschka, E. 1994, *Icarus*, 111, 174
- Kawahara, H., & Fujii, Y. 2011, *ApJ*, 739, id. L62, 6 pp.
- Knutson, H.A., Charbonneau, D., Allen, L.E., et al. 2007, *Nature*, 447, 183
- Komacek, T. D., & Showman, A.P. 2016, *ApJ*, 821, id. 16, 22 pp.
- Kreidberg, L., & Loeb, A. 2016, *ApJ*, 832, L12
- Kuhn, J.R., Potter, D., Parise, B. 2001, *ApJ*, 553, L189
- Kuhn, J.R., & Berdyugina, S.V., 2015, *Int. J. Astrobiology*, 14, 401
- Kuhn, J.R., Berdyugina, S.V., Langlois, M., Moretto, G., Thiébaud, E., Harlinton, C., Halliday, D. 2014, *SPIE Proc.*, 9145, id. 91451G, 8 pp.
- Langlois, M., Vigan, A., Dohlen, K., et al. 2014, *SPIE Proc.*, 9147, id. 91479P, 8 pp.
- Langlois, M. 2017, private communication
- McClatchey, R., Fenn, R., Selby, J., Volz, F., & Garing, J. 1972, *A&A*, Optical Properties of the Atmosphere, AFCRL-72.0497 (US Air Force Cambridge Research Labs)
- Moretto, G., Kuhn, J.R., Thiébaud, E., Langlois, M., Berdyugina, S.V., Harlinton, C., Halliday, D. 2014, *SPIE Proc.*, 9145, id. 91451L, 9 pp.
- Oppenheimer, B.R., Brenner, D., Hinkley, S., et al. 2008, *ApJ*, 679, 1574
- Patat, F. 2008, *A&A*, 481, 575
- Sagan, C., & Khare, B. 1979, *Nature*, 277, 102
- Schwartz, J. C., Sekowski, C., Haggard, H. M., Palle, E., Cowan, N. B., 2016, *MNRAS*, 457, 926
- Simon, A.A., Wong, M.H., Orton, G.S. 2015, *ApJ*, 812, id. 55, 8 pp.
- Snellen, I.A.G., de Mooij, E.J.W., Albrecht, S. 2009, *Nature*, 459, 543
- Sobolev, V.V. 1956, *Radiative Transfer in Stellar and Planetary Atmospheres*, Moscow